Journal of Materials Chemistry C

ROYAL SOCIETY OF CHEMISTRY

PAPER

View Article Online
View Journal

Cite this: DOI: 10.1039/d5tc04129e

Salt complexation drives liquid crystalline self-assembly in crown ether–amino acid hybrids†

Aileen R. Raab,*[a] Tanja Robin Grießer,[a] Daniel Rück,[a] Zhuoqing Li,[bc] Anna Zens,[a] Johanna R. Bruckner,*[f] Patrick Huber,[bc] Andreas Schönhals,[de] Paulina Szymoniak*[d] and Sabine Laschat*[a]

Received 21st November 2025,
Accepted 5th February 2026

DOI: 10.1039/d5tc04129e

rsc.li/materials-c

Crown ether–amino acid hybrids represent a promising class of amphiphilic molecules combining ion recognition with self-assembly capabilities. Despite extensive studies on their binding properties, the influence of inorganic salt complexation on their liquid crystalline behaviour remains underexplored. Here we synthesized amphiphilic [18]-crown-6 derivatives of L-dihydroxyphenylalanine and tetrahydroisoquinoline analogues, systematically investigating the effects of alkyl chain length and salt type on mesophase formation. Complexation with various salts induced liquid crystalline phases, transitioning from smectic A to columnar hexagonal structures as anion size and alkyl chain length increased. Structural analyses and electron density mapping revealed assembly into charged superdiscs forming columnar stacks with tunable ion channels. Broadband dielectric spectroscopy highlighted differences in molecular mobility and conductivity linked to molecular design. These findings establish salt complexation as a key strategy to control self-assembly and ion transport in crown ether–amino acid hybrids, advancing their potential in responsive soft materials and ion-conductive applications.

1. Introduction

Hybrid materials combining crown ethers and amino acids are highly attractive from several perspectives. The ability of crown ethers to form supramolecular complexes with metal salts as well as amino acid and peptide derivatives is useful for chiral separation, molecular recognition and sensing applications. Most of the work has exploited the binding affinities of crown ethers for ammonium and guanidinium units of amino acids and peptides in order to develop chiral stationary phases for HPLC,[1–14] supercritical fluid chromatography[15,16] or capillary electrophoresis.[17,18] Other reports dealt with chiral recognition in solution monitored by colorimetry,[19] guided ion beam mass spectrometry,[20,21] luminescence[22,23] and NMR[24,25] among other methods. Supramolecular interactions between amino acids and crown ethers were also utilized for chiral NMR shift agents.[26,27] The underlying proton transfer has been studied both experimentally and theoretically,[28–30] resulting in the development of mono- or (hetero)ditopic receptors,[31,32] liquid membranes,[23] optical,[33] MRI[34,35] and electrochemical sensors.[36,37] Moreover, the selective ion recognition of crown ethers towards small spherical cations has inspired the development of Li^+ ion receptors[38] and ionophores for model membranes[39–42] as well as ion conductors.[43,44]

Despite this wealth of information on materials based on crown ether/amino acid interactions and reported liquid crystalline crown ethers[38,43,45–62] and mesogenic amino acids,[63–74] surprisingly little is known about liquid crystalline hybrids combining both crown ethers and amino acid entities in one molecular scaffold. Such a combination might lead to novel properties of the hybrid materials, such as ionic conductivity caused by the anions, while the chiral amphiphilic amino acid moiety should self-assemble into mesophases with long-range orientational order.

Depending on the presence or absence of charge, mesophase stabilization may arise from Coulomb interactions, van der Waals forces, π–π stacking of aromatic units, hydrogen bonding, and free-volume minimization, which together drive the nanosegregation of immiscible parts. In an earlier study on liquid crystals (LCs) derived from crown ether–amino acid hybrids, we demonstrated that the presence, number, and

[a] Universität Stuttgart, Institut für Organische Chemie, Pfaffenwaldring 55, 70569 Stuttgart, Germany. E-mail: sabine.laschat@oc.uni-stuttgart.de, aileen-rebecca.raab@oc.uni-stuttgart.de
[b] Hamburg University of Technology, Institute for Materials and X-ray Physics, Denickestr. 15, 21073 Hamburg, Germany
[c] Centre for X-ray and Nano Science CXNS, Deutsches Elektronen-Synchrotron DESY, Notkestr. 85, 22607 Hamburg, Germany
[d] Bundesanstalt für Materialforschung und -prüfung, Unter den Eichen 87, 12205 Berlin, Germany. E-mail: paulina.szymoniak@bam.de
[e] Technische Universität Berlin, Institut für Chemie, Straße des 17. Juni 135, 10623 Berlin, Germany
[f] Universität Stuttgart, Institut für Physikalische Chemie, Pfaffenwaldring 55, 70569 Stuttgart, Germany. E-mail: johanna.bruckner@ipc.uni-stuttgart.de

† Dedicated to Professor Gerhard Erker on the occasion of his 80th birthday.

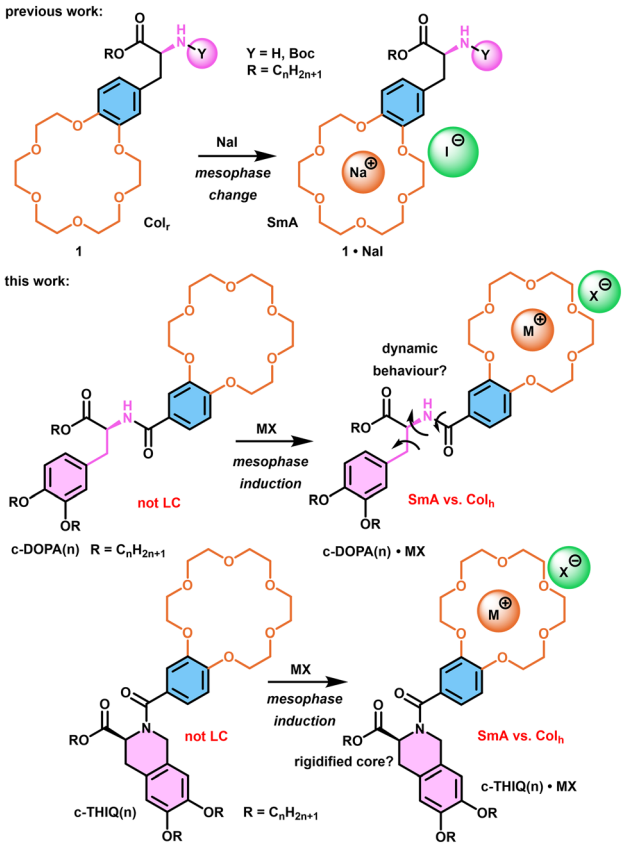

Fig. 1 Our previous work on ionic liquid crystals derived from crown ether–amino acid hybrids (top),[64] and the current work on **DOPA(*n*)** and **THIQ(*n*)** based crown ether hybrids (bottom).

position of charges exerted a pronounced influence on the mesomorphic properties of these hybrid materials.[64] In this previous work the crown ether was directly connected with the aryl unit of the amino acid **1** (Fig. 1). Complexation with NaI changed the columnar rectangular (Col_r) mesophase of **1** to a smectic A (SmA) mesophase for **1·NaI.**

We recently published the dynamical properties and conductivity of L-dihydroxyphenylalanine (L-DOPA)-based guanidinium chlorides, which result from their self-assembly into superdiscs in Col_h phases.[75]

Here we demonstrate for the first time, that the salt complexation of crown ether amino acid hybrids is essential for liquid crystalline self-assembly and also controls their conductive behaviour. For this purpose, we designed the amphiphilic hybrids **c-DOPA(*n*)** consisting of an *N*-terminally bound [18]-crown-6 unit and three flexible alkyl side chains with equal chain length (n = number of carbon atoms per chain) at the C-terminal ester and catechol ether groups of the amino acid DOPA (Fig. 1). To obtain structurally related hybrids with reduced conformational flexibility of the amino acid scaffold, the corresponding rigid tetrahydroisoquinoline crown ether hybrids **c-THIQ(*n*)** were synthesized. The synthesized hybrids and their salt complexes **c-DOPA(*n*)·MX**, **c-THIQ(*n*)·MX** were investigated by polarizing optical microscopy (POM), differential scanning calorimetry (DSC) and X-ray diffraction (XRD) to characterize the mesophase behaviour. The self-assembly of the molecules into mesophases is governed not only by intermolecular interactions but also by molecular mobility.[67,75,76] Therefore, the molecular mobility for selected compounds was further investigated by broadband dielectric spectroscopy. Moreover, as the electrical conductivity of these ionic compounds is essential for applications, this property is also considered for the same selected compounds.

2. Results and discussion

2.1. Synthesis

As outlined in Fig. 2 mesogens **DOPA(*n*)** and **THIQ(*n*)** were prepared from enantiopure L-DOPA **2**. Thus, L-DOPA **2** was protected with Boc_2O in the presence of NEt_3, followed by a one-pot, base-catalysed etherification/esterification with the corresponding *n*-alkyl bromides in the presence of K_2CO_3 and NaI. The removal of the Boc group with TFA results in **DOPA(*n*)** (n = 12, 14, 16) in yields of 43–74% over 3 steps.[65] **DOPA(*n*)** were then reacted with [18]crown-6-benzoic acid **[18]c-6-OH** in the presence of ethylene diamine carbodiimide hydrochloride (EDC···HCl) and 4-(dimethylamino) pyridinium 4-toluene-sulfonate (DPTS) as well as hydroxybenzotriazole monohydrate ($HOBt·H_2O$) to the amides **c-DOPA(*n*)** in yields of 18–84%.

For the synthesis of **c-THIQ(*n*)**, a Pictet–Spengler reaction with aqueous formaldehyde and 0.5 N H_2SO_4 was carried out in 77% yield. Compound **3** was then converted by a similar sequence as described for the **DOPA(*n*)** series to **c-THIQ(*n*)** in yields of 51–65% over 4 steps. Complexation with different salts (MX = KSCN, NaI, KI, $NaBF_4$, KBF_4, KPF_6) provided the materials **c-DOPA(*n*)·MX** in yields of 83–98% and **c-THIQ(*n*)·KPF_6** in yields 83–99%.

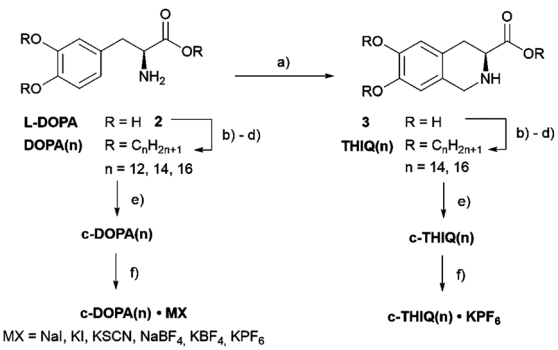

Fig. 2 Synthesis of amino acid and tetrahydroisoquinoline crown ether hybrids and their complexes: (a) CH_2O (37%), 0.5 N H_2SO_4, 8 h, r.t.; (b) Boc_2O, NEt_3, acetone/water (1 : 1), 24 h, r.t.; (c) *n*-BrC_nH_{2n+1}, K_2CO_3, NaI, MeCN, 4 d, reflux; (d) TFA, CH_2Cl_2, 18 h, r.t.; (e) EDC·HCl, $HOBt·H_2O$, DPTS, **[18]c-6-OH**, NEt_3, CH_2Cl_2, 2 d, reflux, (f) MX, CH_2Cl_2/MeOH (1 : 1), 24 h, r.t.

2.2. Thermotropic properties

Investigation of the hybrids by POM suggested a strong dependence of the mesomorphic properties of the complexes on both salts and side chain lengths. While members of the salt-free series **c-DOPA(*n*)**, **c-THIQ(*n*)** did not show liquid crystalline properties, for the complexes **c-DOPA(*n*)·MX** (MX = KSCN, NaI, KI, $NaBF_4$ and KPF_6) and **c-THIQ(*n*)·MX** textures were observed, which indicated the presence of a liquid crystalline phase.

For the **c-DOPA(12)·MX** series with short alkyl chains (Fig. 3, top row, from left to right) **c-DOPA(12)·KSCN** with the smallest anion size showed predominantly homeotropic regions with fine fan-shaped textures and focal conic defect textures, which are typical for SmA phases. Complex **c-DOPA(12)·NaI** showed mostly homeotropic regions with fine Maltese crosses, while the KI-complex features fan-shaped textures. The textures of both iodide complexes are typical for SmA as well. The textures of **c-DOPA(12)·$NaBF_4$** resemble those observed for **c-DOPA(12)·KI**. Therefore, we assume a SmA phase for **c-DOPA(12)·$NaBF_4$**. Complex **c-DOPA(12)·KPF_6** with the largest anion exhibited broad fan-shaped textures. Thus, the whole **c-DOPA(12)·MX** series exhibited SmA phases.

For the **c-DOPA(14)·MX** series with medium chain length similar textures were observed (Fig. 3, middle row, from left to right). **c-DOPA(14)·KSCN** and **c-DOPA(14)·NaI** featured predominantly homeotropic regions with fine uncharacteristic textures that resemble bâtonnets and small Maltese crosses, respectively. Both **c-DOPA(14)·KI** and **c-DOPA(14)·$NaBF_4$** featured fan-shaped textures. Therefore, these complexes also were assigned to form a SmA phase. However, the textures of the complex **c-DOPA(14)·KPF_6** were significantly different from that observed for the other complexes of the **c-DOPA(14)·MX** series. The spherulitic textures and dendritic growth indicate a columnar hexagonal (Col_h) mesophase. This suggested a change of the type of the mesophase within the **c-DOPA(14)·MX** series from a SmA to a Col_h mesophase with increasing anion size. The preference to form columnar hexagonal mesophases instead of layered phases for ionic liquid crystals with large anions like PF_6 has been previously reported by Neidhardt.[63]

For the **c-DOPA(16)·MX** series with the longest alkyl chains (Fig. 3, bottom row) spherulitic textures were observed for the NaI, KI, KSCN and KPF_6 complexes. Additionally dendritic growth was observed for the complex **c-DOPA(16)·KPF_6**. **c-DOPA(14)·$NaBF_4$** complex showed fan-shaped focal conic textures with straight line defects, which are characteristic for columnar hexagonal phases. Therefore, the mesophase types of all complexes in this series were assigned to Col_h phases.

Tetrahydroisoquinoline derivative **c-THIQ(14)·KPF_6** displayed homeotropic regions featuring small Maltese crosses, indicating a SmA phase (Fig. S99). For **c-THIQ(16)·KPF_6** spherulitic textures with dendritic growth were observed (Fig. S99b), which are typical of the Col_h phase and similar to the textures for **c-DOPA(14)·KPF_6** and **c-DOPA(16)·KPF_6** (Fig. 3, middle right and bottom right), respectively.

DSC results summarized in Table 1 confirmed that both salt-free DOPA hybrids **c-DOPA(*n*)** and THIQ hybrids **c-THIQ(*n*)** were not liquid crystalline for the considered chain lengths with n = 12, 14 and 16 (entries 1, 8, 15, 21). The melting points of **c-DOPA(*n*)** occurred at higher temperatures compared to **c-THIQ(*n*)** (n = 14, 16) and did not dependent on the side chain length, whereas the melting temperatures for **c-THIQ(*n*)** increased with increasing n. The complexation of the crown ether unit with salt had a pronounced influence on the melting

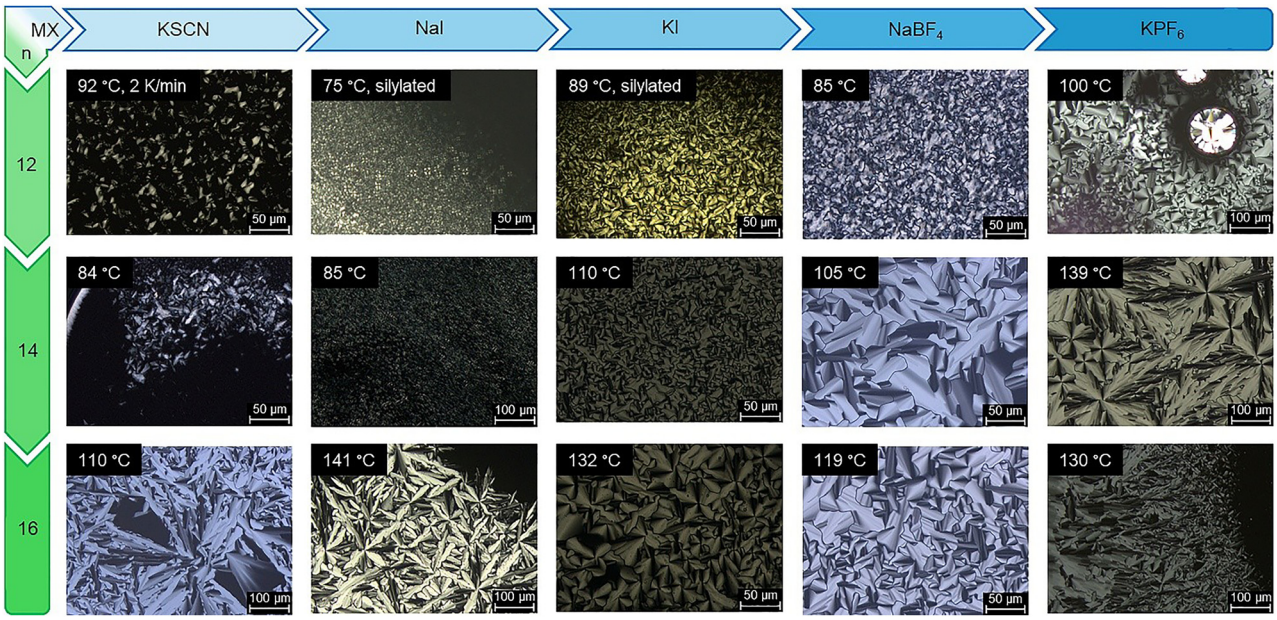

Fig. 3 Textures of the **c-DOPA(*n*)·MX** complexes during cooling observed by polarizing optical microscopy (crossed polarizer), unless otherwise stated on untreated slides with cooling rate: 1 K min^{-1}.

Table 1 Transition temperatures (onset) and enthalpies of the amino acid crown ether hybrids **c-DOPA(*n*)**, **c-THIQ(*n*)** and complexes **c-DOPA(*n*)·MX** and **c-THIQ(*n*)·KPF$_6$** in the 3rd cooling cycle, cooling rate: 5 K min^{-1}

#	*n*	MX	Temperature/°C (enthalpy in kJ mol^{-1})[c]	
c-DOPA(*n*)·MX				
(1)	12	—	Cr 100 (70.6) I	[a]
(2)	12	KSCN	G 61 SmA 91 (1.6) I	
(3)	12	NaI	G 81 SmA 83 (1.0) I	
(4)	12	KI	G 63 SmA 77 (1.2) I	
(5)	12	$NaBF_4$	Cr −19 (2.6) G 53 SmA 115 (0.1) I	[b]
(6)	12	KBF_4	Cr 97 (61.1) I	[a]
(7)	12	KPF_6	G 69 SmA 101 (0.4) I	
(8)	14	—	Cr 101 (70.0) I	[a]
(9)	14	KSCN	G 61 SmA 88 (1.2) I	
(10)	14	NaI	G 81 SmA 83 (1.0) I	
(11)	14	KI	G 57 SmA 98 (0.4) I	
(12)	14	$NaBF_4$	Cr 12 (2.2) G 58 SmA 112 (0.5) I	
(13)	14	KBF_4	Cr 99 (69.1) I	[a]
(14)	14	KPF_6	G 57 Col_h 134 (0.8) I	
(15)	16	—	Cr 100 (49.1) I	[a]
(16)	16	KSCN	Cr 53 (17.3) Col_h 106 (0.6) I	
(17)	16	NaI	Cr 22 (13.8) G 75 Col_h 137 (0.2) I	
(18)	16	KI	Cr 30 (17.5) G 54 Col_h 116 (0.4) I	
(19)	16	$NaBF_4$	Cr 34 (28.1) G 50 Col_h 122 (0.5) I	
(20)	16	KPF_6	Cr 28 (18.0) G 69 Col_h 133 (0.4) I	
c-THIQ(*n*)·MX				
(21)	14	—	Cr 33 (35.0) I	[a]
(22)	14	KPF_6	G 65 SmA 112 (0.4) I	
(23)	16	—	Cr 49 (62.6) I	[a]
(24)	16	KPF_6	Cr 31 (18.1) G 54 Col_h 132 (0.4) I	

[a] The results of the 1st cooling cycle are listed. [b] The results of the 6th cooling cycle are listed. [c] The following phases were observed Cr: crystal, I: isotropic phase, G: glass, SmA: smectic A, Col_h: hexagonal columnar.

behaviour. Except for non-mesomorphic **c-DOPA(*n*)·KBF$_4$** (*n* = 12, 14) (entries 6, 13) all other salt complexes exhibited a liquid crystalline behaviour.

For the **c-DOPA(*n*)·MX** series, enantiotropic mesomorphism was observed for *n* = 12 with NaI and KPF_6 (entries 3, 7), for *n* = 14 with NaI, $NaBF_4$ and KPF_6 (entries 10, 12, 14), and for *n* = 16 with KSCN, NaI, KI, $NaBF_4$ and KPF_6 (entries 16–20). In contrast, monotropic mesomorphism was detected for *n* = 12 with KSCN, KI and $NaBF_4$ (entries 2, 4, 5) and for *n* = 14 with KSCN, and KI (entries 9, 11). For **c-THIQ(*n*)·MX**, enantiotropic mesomorphism was observed for *n* = 14 and 16 with KPF_6 (entries 22, 24). The cation seems to play some role in the mesomorphic properties. Despite the one hundred times higher association constant of the potassium cation with a [18]-crown-6 ether as compared to that of the sodium cation,[77,78] the mesophases of **c-DOPA(12)·KI** and **c-DOPA(14)·KI** were only monotropic, while the corresponding sodium complexes **c-DOPA(12)·NaI** and **c-DOPA(14)·NaI** were enantiotropic. The absence of mesomorphism for **c-DOPA(*n*)·KBF$_4$** (*n* = 12, 14) might be due to the combination of the soft potassium cation with the hard tetrafluoroborate anion (Table S7, SI), which destabilized the mesophase[79–82] (for all DSC curves see Fig. S96–S101, SI).

The complexation of **c-DOPA(*n*)** with metal salts resulted in significant decrease of the glass transition temperature, with the exception of the KBF_4 derivatives (Fig. 4a and b). As

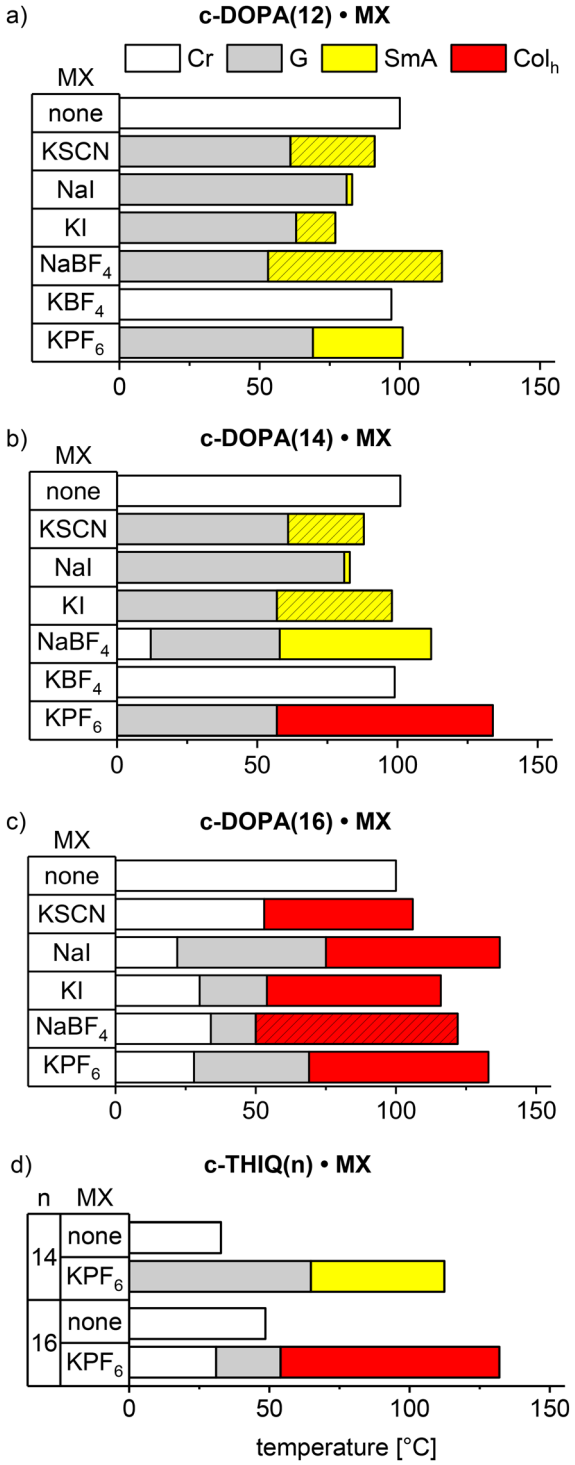

Fig. 4 Mesophase ranges of crown ether complexes **c-DOPA(*n*)·MX** for (a) *n* = 12, (b) *n* = 14, (c) *n* = 16 as well as (d) **c-THIQ(*n*)·MX** in agreement with Table 1, monotropic phases are dashed, cooling rate: 5 K min^{-1}.

c-DOPA(*n*) (*n* = 12, 14) and the corresponding complexes **c-DOPA(*n*)·KBF$_4$** showed almost identical phase transitions in the DSC curves, we checked complex formation *via* ^{19}F NMR. Initial attempts to record ^{19}F NMR spectra of KBF_4 or $NaBF_4$ in $CDCl_3$ were unsuccessful due to insolubility of the salts. In

contrast, the respective complexes **c-DOPA(*n*)·KBF$_4$** and **c-DOPA(*n*)·NaBF$_4$** (n = 12, 14) were soluble and allowed ^{19}F NMR measurements in $CDCl_3$. In addition, ^{19}F NMR spectra of pure KBF_4 and $NaBF_4$ in D_2O were measured (Fig. S92 and S93). The resulting ^{19}F signals differ clearly from those of **c-DOPA(*n*)·KBF$_4$** and **c-DOPA(*n*)·NaBF$_4$** (n = 12, 14), further supporting complex formation (Fig. S55, S70 as well as Fig. S52, S67). Regarding changes of ^{1}H NMR shifts see Fig. S94, S95. For the two series **c-DOPA(12)·MX** and **c-DOPA(14)·MX** a combination of hard anions with hard cations (MX = $NaBF_4$) or soft anions with soft cations (MX = KSCN, KI) reduced the glass transition temperature, stabilizing the mesophase, while a combination of soft anions with hard cations (MX = NaI) destabilized the mesophase, resulting in higher glass transition temperatures and mesophase ranges of only 2 K. This is likely due to enhanced nanosegregation of the mesogens with stronger interactions of hard-hard or soft-soft ion pairs (for the polarizability of the ions see Table S7). By further cooling of **c-DOPA(12)·NaBF$_4$** after vitrification of the sample a crystallization is also observed at −19 °C (Fig. S101a). The other complexes were only cooled to 0 °C, hence we assume they exhibit a similar crystallisation in a comparable temperature range. Additionally, for **c-DOPA(14)·NaBF$_4$** a crystallization also seems to occur below the glass transition temperature (see Fig. S103a).

For the potassium complexes **c-DOPA(16)·KX** (KX = KSCN, KI, KPF_6) the glass transition temperatures increased with increasing anion size, while decreasing with increasing anion size for the sodium complexes **c-DOPA(16)·NaX** (NaX = NaI, $NaBF_4$) (Fig. 4c). Except for the KPF_6-complexes the glass transition temperatures or melting point of the **c-DOPA(16)·MX** series were observed at lower temperatures than of the **c-DOPA(14)·MX** series due to the change of the mesophase type from SmA to Col_h. Furthermore for **c-DOPA(16)·MX** (MX = KSCN, NaI, KI, $NaBF_4$ and KPF_6) a broadened crystallization transition was detected below the glass transition in the range of 22–34 °C (see Fig. 4c and Fig. S104). If the samples were completely vitrified a crystallisation at lower temperature should be suppressed, due to the restricted mobility of the frozen molecules. This indicates that during cooling first partial vitrification of the sample occurs due to freezing of the alkyl chains. Upon further decrease of the temperature the hydrophilic part of the hybrid materials finally crystallizes.

Complexation of **c-DOPA(*n*)** with metal salts resulted in decreased clearing points in the n = 12, 14 series compared to the melting point of the non-complexed compounds, except for the KPF_6 and the $NaBF_4$ derivatives (Fig. 4a and b). However, no general trend regarding anion size was visible. The lowest clearing transition was detected for **c-DOPA(12)·NaI**. In contrast, for the **c-DOPA(16)·MX** series the temperatures of the clearing transition increased significantly upon complexation. Clearing temperatures increased with increasing anion size resulting in broad mesophases with 49–102 K phase widths except for **c-DOPA(16)·NaI** (Fig. 4c).

Comparison of complexes **c-DOPA(*n*)·KPF$_6$** revealed decreasing glass and increased clearing temperatures with increasing chain length, resulting in broader temperature ranges of the mesophases (64–77 K) for n = 14, 16 in the Col_h phase compared to 32 K for n = 12 in the SmA phase. In case of **c-THIQ(*n*)·KPF$_6$** glass transitions temperatures increased slightly with increasing n, while clearing transitions increased significantly, resulting in temperature ranges of the mesophases of 47 K for n = 14 in the SmA phase and 70 K for n = 16 in the Col_h phase. It should be noted that the core rigidity of **c-DOPA(*n*)** *versus* **c-THIQ(*n*)** is not the only parameter that contributes to the thermal stabilization of LC phases and molecular assembled structures. In addition, the presence (in case of **c-DOPA(*n*)**) or absence (in case of **c-THIQ(*n*)**) of hydrogen bonds seems to play a major role as well. Thus, hydrogen bonds stabilize the crystalline phase of **c-DOPA(*n*)** (n = 14, 16), resulting in much higher melting temperatures as compared to **c-THIQ(*n*)**. The hydrogen bonding interactions are weakened for the corresponding KPF_6 complexes, likely due to the high fluidity of the molecules in the mesophase and the disorder in the glassy state. Fluidity and disorder become more relevant with increasing chain lengths. Thus, no significant stabilization of the mesophase of **c-DOPA(16)·KPF$_6$** compared to **c-THIQ(16)·KPF$_6$** was observed in contrast to the higher clearing temperature and broader mesophase range of **c-DOPA(14)·KPF$_6$** as compared to **c-THIQ(14)·KPF$_6$**.

Additionally in the heating cycles of **c-DOPA(14)·NaBF$_4$**, **c-DOPA(16)·NaI**, **c-DOPA(16)·NaBF$_4$** and **c-THIQ(16)·KPF$_6$** Cr → Cr transitions were observed (Fig. S103a, S104c and S105d). Especially the glass transitions are hardly visible. Typical examples are **c-DOPA(12)·KPF$_6$** (Fig. 5a), **c-DOPA(14)·KPF$_6$** (Fig. 5b) and **c-DOPA(16)·KPF$_6$** (Fig. 5c), where the glass transition in the cooling cycle is barely detectable.

Additionally, measurements using fast scanning calorimetry (FSC) performed with a Flash DSC with high heating rates of up to 10.000 K s^{-1} on **c-DOPA(16)·KPF$_6$** and **c-THIQ(16)·KPF$_6$** also showed a glass transition above the crystallisation during heating (Fig. S181 and S182). Due to the high heating rates the change of the heat flow at the glass transition is enhanced by FSC compared to conventional DSC measurements. Thus, it can be surmised that the amino acid-based hybrids **c-DOPA(*n*)·MX** and **c-THIQ(*n*)·MX** exhibit a mesophase (M) → G transition during cooling, which is accompanied by a crystallisation (G → Cr). The only exception of this observation is **c-DOPA(16)·KSCN**, which crystallizes immediately from the mesophase during cooling and does not form a glass.

In order to assign phase geometries, XRD studies were carried out. Smectic phases, identified based on POM textures, showed a distinct small angle reflection assigned to the (001) reflex of a smectic structure (Fig. 6b). For the KI-complexes **c-DOPA(12)·KI** and **c-DOPA(14)·KI** a second distinct reflection was observed in the small angle section, which was assigned to the (002) reflex (Fig. 6a and Fig. S105, S106, S115–S117) that originates from the locally increased electron density of the comparably electron-rich KI.[83] In the wide-angle region a broad halo was visible for all smectic complexes, which was caused by the average distance of the liquid-like alkyl side chains (Fig. S102–S122 and S158–S161).[84] Using Bragg's law the

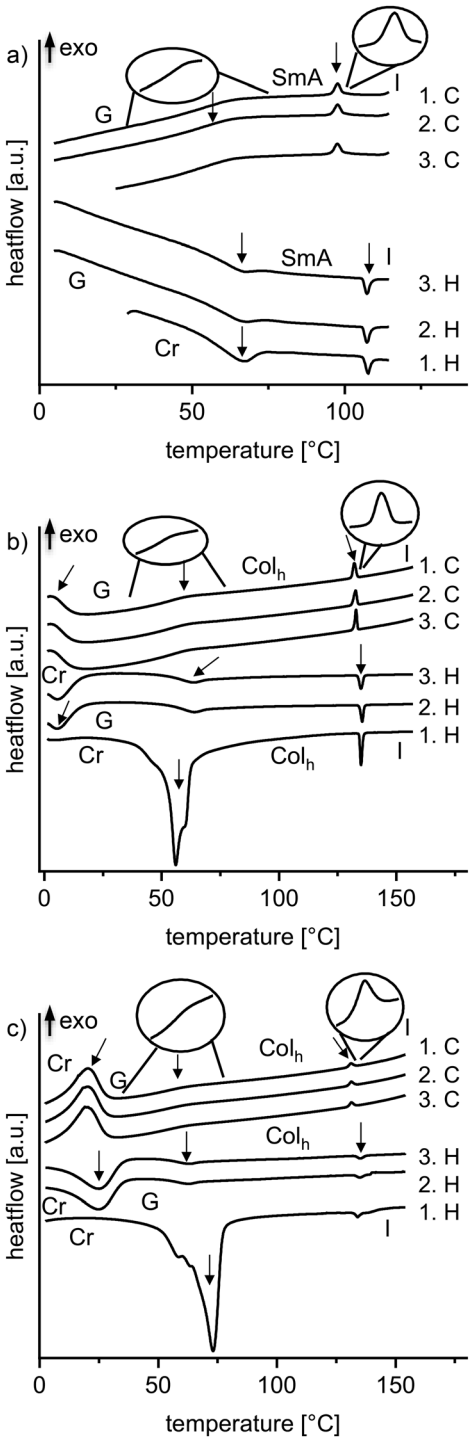

Fig. 5 Representative DSC thermograms of **c-DOPA(*n*)·KPF$_6$** with (a) n = 12 (b) n = 14 (c) n = 16, heating and cooling rate: 5 K min^{-1}.

periodicity distance d was determined in dependence of the temperature from the reflexes of the SAXS experiments by the following equation:

$$d = \frac{\lambda}{2 \cdot \sin(\theta)} \quad (1)$$

with λ, the wavelength of the X-ray beam and 2θ, the scattering

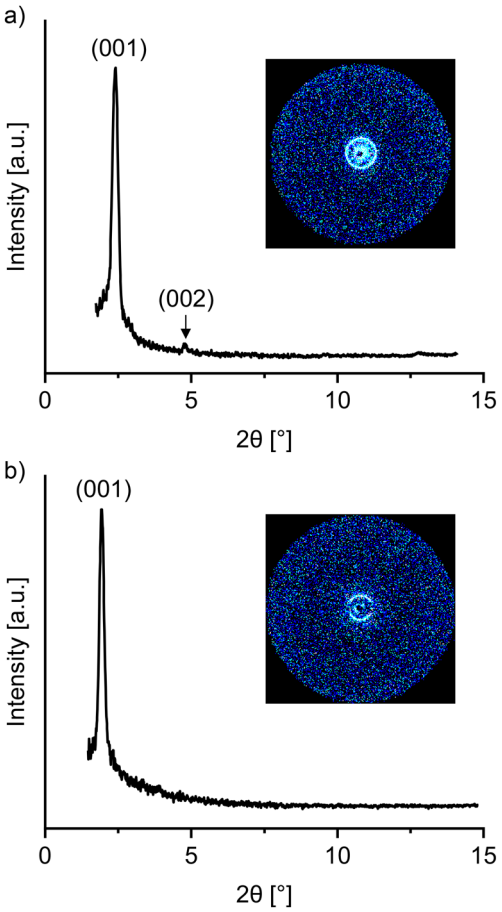

Fig. 6 (a) SAXS diffractogram of **c-DOPA(12)·KI** at 70 °C (inset: 2D diffraction pattern) and (b) SAXS diffractogram of **c-DOPA(12)·KPF$_6$** at 75 °C (inset: 2D diffraction pattern) during cooling from the isotropic phase.

angle. In case of smectic phases, d calculated from the (001) reflex, doubles as the smectic layer spacing d_{obs}.

For **c-DOPA(12)·KI** the ratio of the 2θ-values of the (001) and (002) reflexes was 1 : 2 confirming a SmA phase with a layer spacing of 36.9 Å. Considering the calculated molecular lengths of **c-DOPA(12)** L_{calc} = 29.5 Å (obtained *via* Avogadro molecular modelling software),[85] the ratio d_{obs}/L_{calc} = 1.25 suggests the presence of a SmA$_d$ phase, *i.e.* a bilayer organization of the crown ether amino acid hybrids with a strong degree of interdigitation of the alkyl chains as well as at least a partial overlap of the hydrophilic region of the mesogens, *e.g.* by stacking of the crown ether units.

Similar ratios for the 2θ-values were obtained for **c-DOPA(14)·KI** supporting the initial assignments of a SmA-type phase for **c-DOPA(12)·MX** (MX = KSCN, NaI, KI, NaBF$_4$, KPF$_6$), **c-DOPA(14)·MX** (MX = KSCN, NaI, KI, NaBF$_4$) as well as **c-THIQ(14)·KPF$_6$**, based on the POM studies (Fig. 3 and Fig. S99). The results are listed in Table 2, the diffractograms are depicted in the SI (Fig. S102–S122 and Fig. S158–S161). The smectic layer spacing d_{obs} increases with increasing chain length. The values of d_{obs} increase with increasing anion size for **c-DOPA(12)·MX** from d_{obs} = 36.9 Å (KI) to 45.1 Å (KPF$_6$) and

Table 2 Calculated and observed values of the distances associated with the observed reflexes in SAXS and WAXS for the liquid crystalline complexes **c-DOPA(*n*)·MX** and **c-THIQ(*n*)·MX** with calculated cell constant *a* and values for *Z* for columnar phases. Broad reflexes are denoted with (br)

n	MX	*T*/°C	Phase type	*hkl*	*d*/Å	Lattice constant *a*/Å and *Z*-value
c-DOPA(*n*)·MX						
12	KSCN	85	SmA_d	001	38.8	—
				halo	4.5 (br)	
12	NaI	77	SmA_d	001	37.9	—
				halo	4.1 (br)	
12	KI	70	SmA_d	001	36.9	—
				002	18.5 (18.4)	
				halo	4.4 (br)	
12	$NaBF_4$	85	SmA_d	001	41.9	—
				halo	4.5 (br)	
12	KPF_6	83	SmA_d	001	45.1	—
				halo	4.1 (br)	
14	KSCN	85	SmA_d	001	39.4	—
				halo	4.5 (br)	
14	NaI	75	SmA_d	001	39.4	—
				halo	4.5 (br)	
14	KI	80	SmA_d	001	40.1	—
				002	20.0 (20.1)	
				halo	4.2 (br)	
14	$NaBF_4$	80	SmA_d	001	46.3	—
				halo	4.4 (br)	
14	KPF_6	60	Col_h	100	49.6	a = 57.2
				110	28.7 (28.6)	Z = 6
				200	24.8 (24.8)	
				halo	4.5 (br)	
16	KSCN	85	Col_h	100	48.7	a = 56.2
				110	28.3 (28.1)	Z = 6
				200	24.3 (24.4)	
				halo	4.6 (br)	
16	NaI	93	Col_h	100	53.7	a = 61.7
				110	30.8 (31.0)	Z = 6
				200	26.9 (26.8)	
				halo	4.4 (br)	
16	KI	80	Col_h	100	53	a = 61.1
				110	30.6 (30.6)	Z = 6
				200	26.7 (26.5)	
				halo	4.5 (br)	
16	$NaBF_4$	80	Col_h	100	47	a = 54.2
				110	27.1 (27.1)	Z = 5
				200	23.7 (23.5)	
				halo	4.6 (br)	
16	KPF_6	74	Col_h	100	56.8	a = 65.6
				110	33.1 (32.8)	Z = 7
				200	28.6 (28.4)	
				halo	4.4 (br)	
c-THIQ(*n*)·MX						
14	KPF_6	80	SmA_d	001	46.3	—
				halo	4.5 (br)	
16	KPF_6	80	Col_h	100	50.6	a = 58.5
				110	29.4 (29.2)	
				200	25.4 (25.3)	
				halo	4.5 (br)	

for **c-DOPA(14)·MX** from d_{obs} = 39.4 Å (KI) to 46.3 Å (KPF_6). Meanwhile **c-THIQ(14)·KPF$_6$** exhibited d_{obs} = 36.4 Å and a d_{obs}/L_{calc} ratio of 1.31 (Fig. S174). The reduction of the layer thickness by addition of the CH_2-bridging unit is related to a change of the molecular shape, which will be discussed below assisted by Fig. 7–9.

For **c-DOPA(14)·MX** with MX = KSCN, NaI and KI a small increase of the layer thickness with increasing temperature was observed (Fig. S175). Such a positive thermal expansion is atypical for SmA phases[86–91] and could be related to a compensating effect of the alkyl chains by strong interdigitation as well as a stronger interaction between neighbouring crown ether units at low temperatures.[92,93] Only for larger anions X = BF_4^-, PF_6^- an increase of the layer thickness with decreasing temperature was observed, which possibly is due to a reduction of stacking interactions between neighbouring crown ether units caused by the larger anions (Fig. S175).

Comparison of the Avogadro-optimized molecular geometry of **c-DOPA(14)** with **c-THIQ(14)** revealed a smaller angle between the DOPA aryl unit and the benzocrown unit as

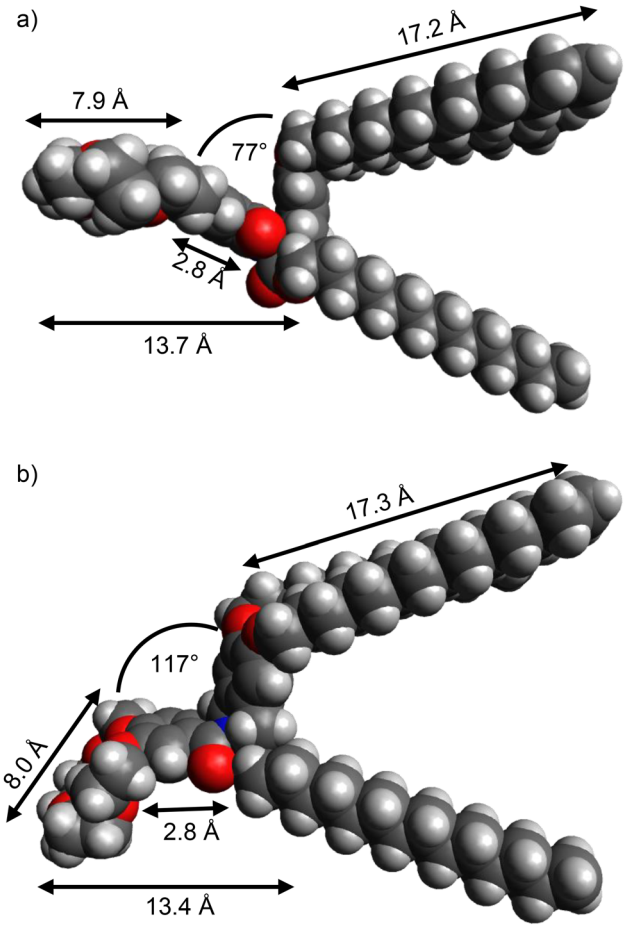

Fig. 7 Optimized molecular geometry of (a) **c-DOPA(14)** and (b) **c-THIQ(14)**.

compared to the angle between the THIQ aryl unit and benzocrown unit respectively (Fig. 7). This results in a larger steric demand of **c-THIQ(*n*)** compared to **c-DOPA(*n*)** in the hydrophilic region, which could accommodate for larger anions like PF_6^- in the smectic mesophase.

Since the KI-complexes exhibited two reflexes in the small angle region the relative electron density distribution $\rho(z)$ in *z*-direction, *i.e.* parallel to the layer normal of the smectic layers, could be calculated with the approximation:

$$\rho(z) \propto \sum_l \sqrt{a_l} \cdot \cos(l \cdot 2\pi \cdot z/d_{obs}) \qquad (2)$$

In this equation, l denotes the value of the corresponding Miller index, a_l represents the intensity of the corresponding reflex (00l) with consideration of the Lorentz correction factor and d_{obs} corresponds to the experimental layer spacing.[94–96] The results are depicted in Fig. 8.

The accuracy of electron density profiles increases with the number of reflexes, hence for these complexes with just two reflexes they will not perfectly fit with regions of differing electron densities. As exemplified for **c-DOPA(14)·KI** the region of higher electron density corresponds to the crown ether units with the free anions connected by phenyl spacers to the

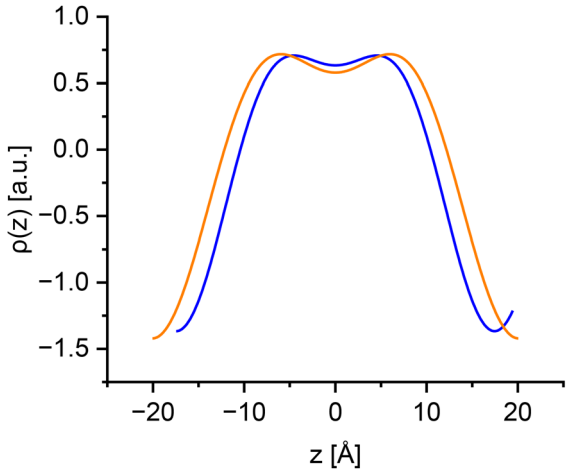

Fig. 8 1D electron density distribution of **c-DOPA(12)·KI** (blue) and **c-DOPA(14)·KI** (orange).

aromatic core. The region with low electron density corresponds to the aliphatic chains of the mesogens, which are interdigitated with the aliphatic chains of the neighbouring smectic layer. The crown ether units are stacked on each other. Based on this proposed molecular arrangement the increase of the layer spacing with larger anions can be explained by a larger steric demand of the anions, which pushes the molecules outwards leading to an undulation of the stacked crown ether units. At the same time, the increase of the layer spacing allows the interdigitated alkyl chains of adjacent layers to decrease their lateral distance which is evident in the reduction of the intralamellar distance referred to as halo in Table 2. The crown ether unit of the **c-THIQ(*n*)** system forms a larger angle to the aromatic core, changing the effective shape of the molecule to a cylindrical form. Thus, the molten alkyl chains are less extended or stronger interdigitated to enable a space filling packing of the molecules in comparison to the c-DOPA molecules which possess a more truncated cone-like shape. This explains the small layer spacing for **c-THIQ(14)·KPF_6** among the KPF_6-complexes.

Accordingly, a proposed molecular arrangement of **c-DOPA(12)·KPF_6** and **c-THIQ(14)·KPF_6** in the SmA_d phase is depicted in Fig. 9.

All complexes, which were assigned Col_h phases based on the textures determined by POM (Fig. 3 and Fig. S99), exhibited three distinct peaks in the small-angle regions (Fig. 10) and a broad halo in the wide-angle region. The 2θ-values of the peaks in the small angle region, which were assigned to the (100), (110) and (200) reflex, had a relation of $1{:}\sqrt{3}{:}2$, confirming a hexagonal columnar (Col_h) phase with *p6mm* space group.

The lattice parameter a was calculated from the periodicity distance d_{100} of the (100) reflex with the equation:

$$a = 2 \cdot d_{100}/\sqrt{3} \qquad (3)$$

and corresponds to the intercolumnar distance.[97,98] Furthermore, for hexagonal lattices the number of molecules Z per cell unit[99,100] can be calculated by using the lattice parameter a and the molecular height h of the column stratum, which was

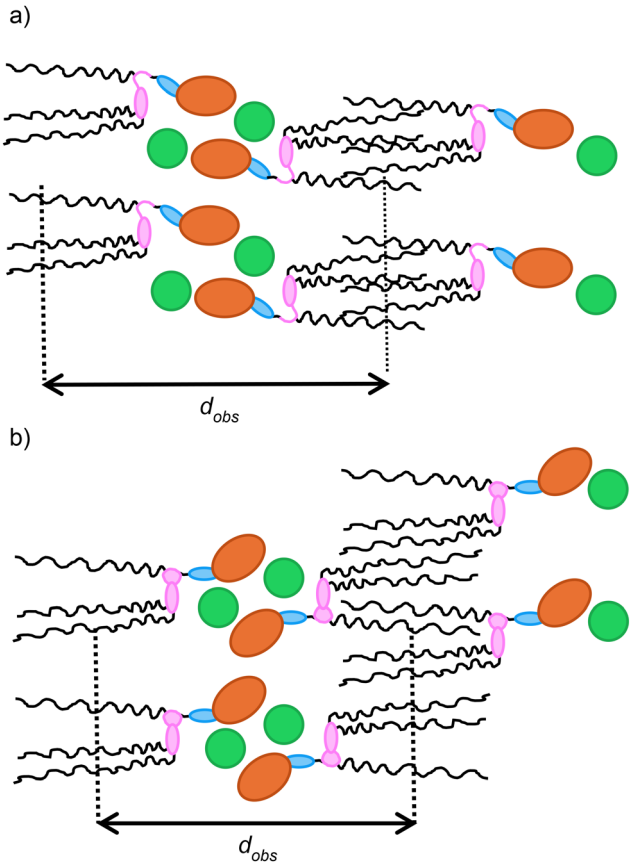

Fig. 9 Proposed packing pattern in the SmA_d mesophase exemplified for (a) **c-DOPA(12)·KPF$_6$** and (b) **c-THIQ(14)·KPF$_6$**. The interdigitation of the aliphatic region with the neighbouring layer is indicated. The crown ether unit is depicted in orange, the phenyl spacer in blue, the mesogenic core in pink and the anion in green.

determined with eqn (1) from the wide-angle halo and corresponds to the molecular thickness, according to

$$Z = \frac{\sqrt{3} \cdot \rho \cdot N_A \cdot h \cdot a^2}{2 \cdot M} \quad (4)$$

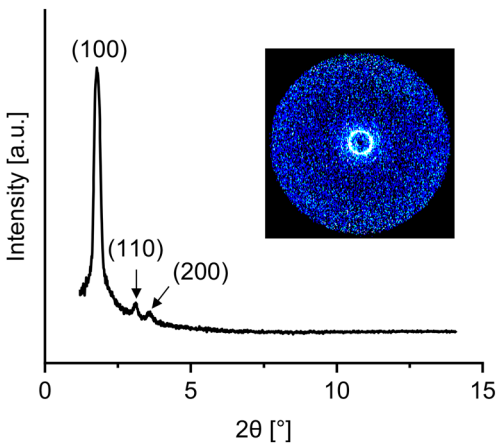

Fig. 10 SAXS diffractogram of **c-DOPA(14)·KPF$_6$** at 60 °C (inset: 2D diffraction pattern) during cooling from the isotropic phase.

N_A corresponds to the Avogadro constant and M the molecular weight of the complex. For organic materials the density ρ typically ranges between 1.0 g cm^{-3} and 1.2 g cm^{-3}.[100] For the calculations a density of 1.0 g cm^{-3} was assumed.

The lattice parameter a of **c-DOPA(n)·KPF$_6$** increased with increasing chain length from a = 57.2 Å (n = 14) to 65.6 Å (n = 16). Despite n = 16 for **c-THIQ(16)·KPF$_6$**, the lattice parameter is only 58.5 Å due to the shorter molecular length caused by the bridging CH_2 group. These correspond to an a/L_{calc} ratio of 1.79 for **c-DOPA(14)·KPF$_6$** and 1.55 for **c-THIQ(16)·KPF$_6$**, revealing a much stronger interdigitation of the alkyl chains of adjacent columns for the latter component. The a/L_{calc} ratios for the **c-DOPA(16)·MX** complexes showed a strong dependence on the salt: for the potassium complexes (KSCN, KI, KPF_6) the a/L_{calc} ratio increased with increasing anion size and decreasing polarizability, ranging from 1.63 (KSCN) to 1.90 (KPF_6) while for the sodium complexes the lattice parameter increased with increasing anion polarizability, with a/L_{calc} ranging from 1.36 ($NaBF_4$) to 1.79 (NaI) (Fig. S176).

All complexes exhibited a negative thermal expansion, with a noticeable decrease of the lattice parameter with increasing temperatures. For example, for **c-DOPA(16)·KPF$_6$** a decreased from 65.6 Å at 70 °C to 59.5 Å at 130 °C (Fig. 11). A similar thermal expansion was previously observed for DOPA-based guanidinium chlorides and could be caused by increased intracolumnar distance between the supramolecular disks at higher temperatures.[67]

Not only the intercolumnar space but also the intracolumnar space was affected by the salt. A comparison of the intracolumnar distances, denoted as halo in Table 2, for the potassium complexes **c-DOPA(16)·KX** with X = SCN$^-$, I$^-$ and PF_6^- showed a decrease of the average distance of the alkyl side chains with increasing anion size and decreasing polarizability. This indicates, similar to the results observed for the SmA_d mesophases, that larger anions, due to their increased space

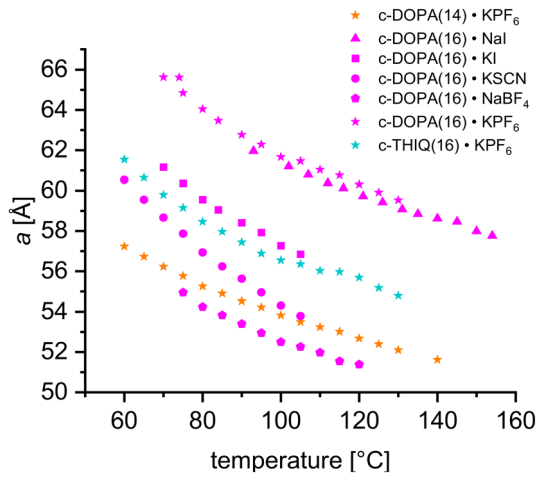

Fig. 11 Temperature dependence of the hexagonal lattice parameter a for **c-DOPA(14)·KPF$_6$** (orange), **c-DOPA(16)·MX** (pink) and **c-THIQ(16)·KPF$_6$** (cyan) with MX = KSCN (dot), NaI (triangle), KI (square), $NaBF_4$ (pentagon), KPF_6 (star).

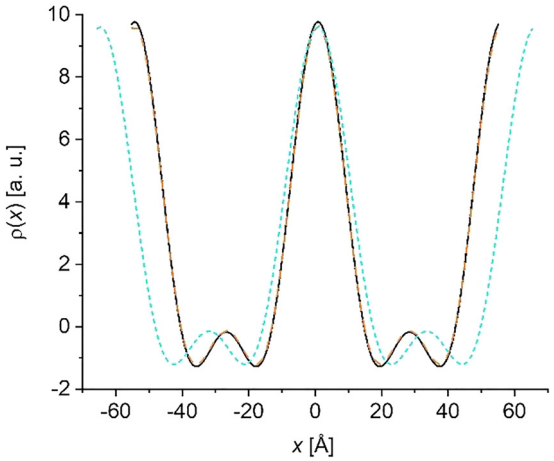

Fig. 12 1D electron density distribution of **c-DOPA(14)·KPF$_6$** (orange), **c-DOPA(16)·KSCN** (black) and **DOPA(16)·KPF$_6$** (cyan) along the unit cell axis.

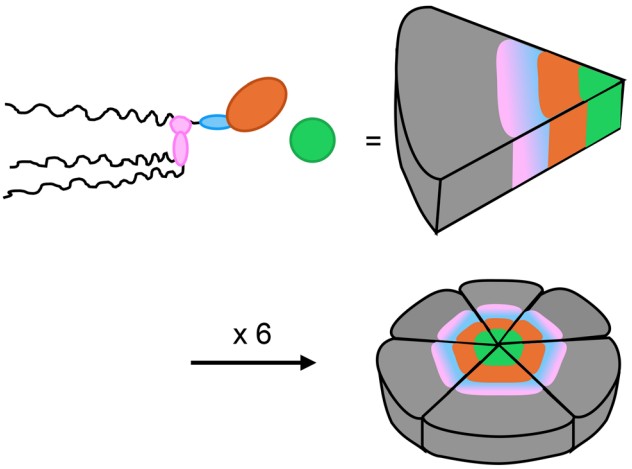

Fig. 13 3D depiction of the proposed self-assembly of **c-THIQ(16)·KPF$_6$** into superdiscs. The crown ether unit is depicted in orange, the phenyl spacer in blue, the mesogenic core in pink and the anion in green.

requirement, push the molecules slightly out of the column centre which results in an increased lattice parameter. As a consequence, the alkyl chains need to spread and flatten to still guarantee a space filling packing, which in turn reduces the intracolumnar distance between the alkyl chains (Fig. S177).

The *Z*-values calculated according to eqn (4) range between 5 and 7. Since for most complexes a value of $Z = 6$ was obtained if the density was merely assumed to be 1.0 g cm^{-3}, we propose for **c-DOPA(14)·KPF$_6$**, **c-DOPA(16)·MX** and **c-THIQ(16)·KPF$_6$** that six molecules of the amino acid or tetrahydroisoquinoline crown ether complexes self-assemble to charged superdiscs with the crown ether cation complexes and anions located in the centre of the column surrounded by the aromatic core of the mesogens similar to the arrangement for DOPA-based ILCs with guanidinium headgroups known in literature (Fig. 13).[65,67,101–111] Space filling between the columns is maintained by the alkyl side chains due to their tendency to maximize London dispersion interactions. Interdigitation and deviation from the *all-trans* configuration of the alkyl chains result in a cell constant larger than the molecular length but significantly smaller than the two-fold molecular length.

For the different complexes the two-dimensional electron density distribution $\rho(xy)$, with the *xy*-plane being orthogonal to the director, was calculated according to

$$\rho(xy) \propto \sum_{hk} \sqrt{a_{hk}} \cdot \cos\left(-\frac{2\pi \cdot (hx + ky)}{a} + \varphi(hk)\right) \qquad (5)$$

with the Miller indices *hkl* (note that $l = 0$ for the 2D hexagonal structure and can thus be omitted), the intensity a_{hk} of the reflex (*hkl*), the calculated lattice parameter a and the phase angle $\phi(hk)$, which can take the values 0 or π and is assigned based on the most plausible outcome of the electron density map.

For the complexes **c-DOPA(14)·KPF$_6$**, **c-DOPA(16)·KSCN** and **DOPA(16)·KPF$_6$** the 1D electron density profiles along the unit cell axis are depicted in Fig. 12. A representative model for the proposed molecular arrangement is depicted in Fig. 13 for **c-THIQ(16)·KPF$_6$**. The region of higher electron density is located in the middle of the column, with an ion channel of the anions located in the centre, which are surrounded by the crown ether units and subsequently the aromatic part of the molecules. The aliphatic chains are located in the intercolumnar space and correspond to the region of lower electron density. Larger anions like PF_6^- require more space in the centre of the column, resulting in a flattening and broadening of the superdiscs. This effect is partially compensated for **c-THIQ(16)·KPF$_6$**, which enables the accommodation of larger anions due to the difference of the shape in the hydrophilic region accommodating for larger anions.

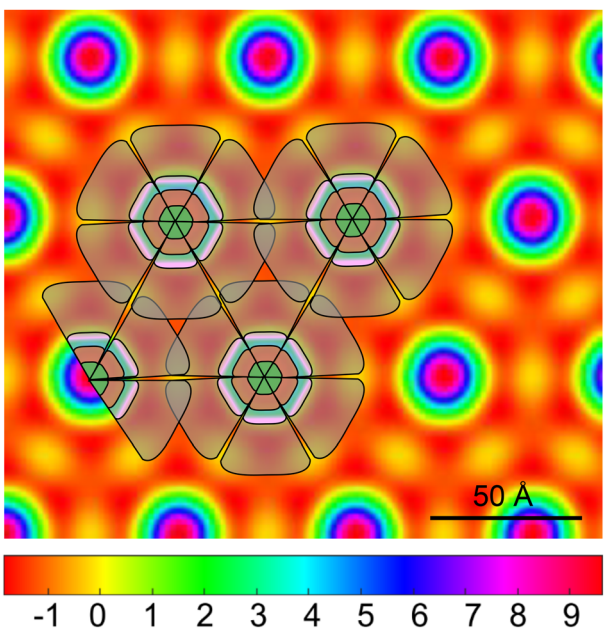

Fig. 14 2D electron density distribution in the *x*,*y*-plane with schematic depiction of the molecular arrangement for **c-THIQ(16)·KPF$_6$** with indicated self-assembly of the superdiscs into a Col$_h$ phase.

The results of the electron density profiles also imply, that the six mesogens of a cell unit do assemble to a flat superdisc like it was proposed for the guanidinium chlorides by Neidhardt.[65] Calculation of a 2D electron density profile reinforce this proposed molecular arrangement, as depicted for **c-THIQ(16)·KPF$_6$** in Fig. 14. Further 2D electron density maps are depicted in Fig. S179. To learn more about the location of the anion, we constructed an electron density difference map by subtracting the electron density distribution of **c-DOPA(16)·NaBF$_4$** from the one of **c-DOPA(16)·NaI** (Fig. S180 and corresponding discussion). This difference map further supports the proposed structure model of anion channels being located in the middle of the columns.

2.3. Retardation measurements

Temperature-dependent optical retardation measurements[112,113] were conducted for **c-THIQ(16)·KPF$_6$** (Fig. 15) and **c-DOPA(16)·KPF$_6$** (Fig. S178) to characterize the collective thermotropic alignment of discotic amino acid crown ether hybrids in cells of different surface hydrophobicity. The experimental setup employed a He–Ne laser (wavelength 632.8 nm) as a linearly polarized light source.

The liquid crystalline powders were heated to approximately 20 °C above the liquid crystalline–isotropic phase transition temperature, then introduced into the bulk cells *via* capillary forces resulting in spontaneous imbibition. The bulk cells consisted of two glass substrates separated by a defined gap of 1.6 μm. The inner surfaces of the glass plates were chemically treated to produce either hydrophilic or hydrophobic surface conditions, thereby imposing distinct anchoring environments for the confined liquid crystals (for details, see Fig. S177). From the optical retardation curves the optical birefringence can be inferred (see SI, Chapter S9).

The retardation curves **c-THIQ(16)·KPF$_6$** allow for the extraction of meaningful information in both anchoring environments, as seen in Fig. 15. In both cases, the optical retardation signal is well-reproducible in the low-temperature regime below 320 K. A distinct transition from the liquid crystalline to the crystalline phase is observed near 315 K for both hydrophilic and hydrophobic surface treatments.

Within the liquid crystalline phase, **c-THIQ(16)·KPF$_6$** also displays signs of a multi-domain structure, as evidenced by moderate fluctuations in the optical retardation signal. Nonetheless, a weak and somewhat broad isotropic to liquid crystalline (I–LC) transition can still be discerned. This transition appears between 400 K and 410 K upon cooling, and between 360 K and 370 K during heating, albeit less sharply defined than the crystalline to liquid crystalline (Cr–LC) transition. The experimental setup does not allow the simultaneous confirmation of the multi-domain structure *via* POM.

The optical retardation response of **c-DOPA(16)·KPF$_6$** (Fig. S178) exhibits irregular fluctuations within a relatively narrow range and lacks reproducibility. This behaviour is likely attributable to weak surface anchoring, leading to the formation of a multi-domain structure within the bulk cell. The presence of randomly oriented domains results in minimal net optical anisotropy, which manifests as a fluctuating and poorly defined optical retardation signal which will not be discussed further.

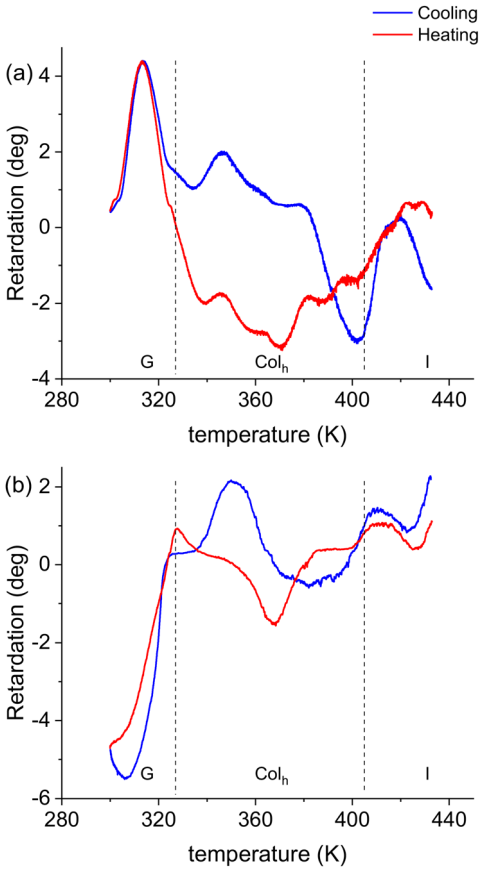

Fig. 15 Optical retardation measurements of **c-THIQ(16)·KPF$_6$** in the bulk state under different surface conditions. (a) corresponds to cells with hydrophilic surface treatment, while (b) shows results for cells with hydrophobic surface treatment; dashed lines indicate phase transitions measured during 3rd cooling measured by DSC.

It is well established that conventional LC materials typically exhibit thermal hysteresis in their phase transitions, where the liquid crystalline to isotropic transition (LC–I) occurs at a higher temperature upon heating and at a lower temperature during cooling. This behaviour arises from the first-order nature of the transition, which involves a discontinuous change in order parameters such as molecular orientation or positional order, and is associated with latent heat and a free energy barrier separating the two phases. Upon heating, the LC phase can persist until a superheating limit is reached, beyond which thermal energy is sufficient to overcome the energy barrier, resulting in a transition to the isotropic phase. During cooling, the isotropic phase may remain metastable below the equilibrium transition temperature until nucleation of the LC phase occurs – often delayed by surface anchoring conditions, defects, or impurities – leading to a lower apparent transition temperature.

However, in the present case, we observe an inverse hysteresis: the LC–Iso transition occurs at a lower temperature during

heating and at a higher temperature during cooling. This atypical behaviour may be attributed to slow relaxation dynamics within the system. For instance, high viscosity, structural defects, or molecular crowding can hinder complete reorganization during the heating cycle, causing the LC structure to lose order prematurely and resulting in an early transition to the isotropic phase. Conversely, during cooling, nucleation of the LC phase may be facilitated by surface anchoring or residual molecular order, causing the transition to occur at a comparatively higher temperature. This reversal of hysteresis thus reflects the complex interplay between kinetic constraints and interfacial effects in the phase behaviour of the material.

The observed difference in collective orientation behaviour between the bridged and non-bridged molecules in the planar LC cell can be primarily attributed to differences in molecular rigidity and shape persistence. The bridged molecule, being structurally more rigid due to its covalent constraint, likely maintains a more anisotropic and well-defined molecular geometry. This rigidity favours stronger and more coherent intermolecular interactions, thereby enhancing long-range orientational order within the cell. In contrast, the non-bridged molecule possesses greater conformational flexibility, which can lead to a broader distribution of molecular orientations and a higher likelihood of forming disordered or multi-domain structures. Additionally, rigid molecules typically have higher elastic constants (especially for splay and bend deformations), making it energetically more favourable for them to adopt uniform alignment under the influence of surface anchoring. In contrast, flexible molecules can more easily distort or accommodate random orientations, resulting in weaker macroscopic birefringence signals due to poor collective alignment.[114,115]

2.4. Dielectric studies

Dielectric investigations were carried out for two samples **c-DOPA(16)·KPF$_6$** and **c-THIQ(16)·KPF$_6$**. These samples were selected for the following reasons: first, both samples have a columnar mesophase which is important for applications like ion or water transport. Second, dielectric spectroscopy will allow to directly investigate the change in the molecular mobility due to the bridged structure in the core of **c-THIQ(16)·KPF$_6$** compared to that of **c-DOPA(16)·KPF$_6$**. Additionally, the electrical conductivity was measured. The dielectric spectrum of **c-THIQ(16)·KPF$_6$** is shown in Fig. 16 as dielectric loss ε'' *versus* frequency and temperature in a 3D representation for the columnar mesophase and the low-temperature phase, which could be identified as a plastic crystalline phase. Plastic crystalline phases are solid-state phases that combine long-range positional order with orientational or conformational mobility of the constituent molecules resulting in detectable molecular mobility.[116] Several dielectric relaxation processes are observed, indicated as peaks in ε'' besides a conductivity contribution. An analogous behaviour was observed for **c-DOPA(16)·KPF$_6$** (Fig. S179).

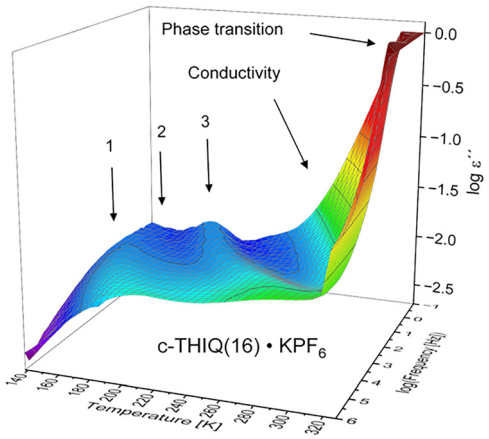

Fig. 16 Dielectric loss *versus* frequency and temperature in a 3D representation for **c-THIQ(16)·KPF$_6$** at lower temperatures. The relaxation processes and the conductivity contributions are marked by arrows.

The relaxation processes were labeled from 1 to 3 in order of increasing temperature. At higher temperatures the dielectric loss increases strongly with decreasing frequency and increasing temperature due to electrical conductivity related to the drift motion of charge carriers like ions and conductivity related processes like Maxwell/Wagner/Sillars and/or electrode polarization. By a derivative approach (conduction free loss)[118] it could be shown that a further relaxation is hidden by the conductivity which is called relaxation process 4 or α-relaxation (see Chapter S10, SI).

The analysis of the dielectric spectra is based on the fitting of the model function of Havriliak-Negami (HN) to the data.[117,119] For details (see Chapter S10, SI). From the fits the frequency of maximal dielectric loss for each process f_p (relaxation rate) is derived.

Fig. 17 depicts the temperature dependence of the relaxation rate f_p *versus* inverse temperature (Arrhenius diagram). The temperature dependence of the relaxation rates for process 1 follows the Arrhenius equation which is given by

$$f_p = f_\infty \exp\left(-\frac{E_A}{RT}\right) \quad (6)$$

Here f_∞ represents the preexponential factor, while E_A denotes the activation energy and R refers to the universal gas constant. The activation energies were estimated to 35.4 kJ mol^{-1} for **c-DOPA(16)·KPF$_6$** and 36.6 kJ mol^{-1} for **c-THIQ(16)·KPF$_6$**. These values can be considered as similar as the error of the activation energy is around 1 kJ mol^{-1}. The values of the activation energy of process 1 indicate a localized molecular process. To assign the molecular origin of this relaxation process data for the γ-relaxation of polyethylene (PE) is included into Fig. 17.[120] The γ-relaxation of PE occurs in a temperature and frequency range similar to that of the process 1 for both **c-DOPA(16)·KPF$_6$** and **c-THIQ(16)·KPF$_6$** with a comparable activation energy. Consequently, it is inferred that the relaxation process 1 of **c-DOPA(16)·KPF$_6$** and **c-THIQ(16)·KPF$_6$** arises from localized

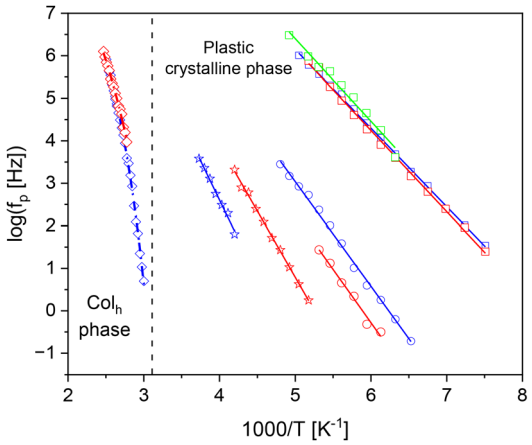

Fig. 17 Temperature dependence of the relaxation rates *versus* inverse temperature: (blue) – **c-DOPA(16)·KPF$_6$**, (red) – **c-THIQ(16)·KPF$_6$**, (green) – data for polyethylene taken from the literature.[117] (squares) – Relaxation process 1, (circles) – relaxation process 2, (asterisk) – relaxation process 3 and (diamonds) – relaxation process 4 (α-relaxation). Solid lines are fits of the Arrhenius equation to the corresponding data. The dashed-dotted line indicate fits of the VFT equation to the corresponding data of the α-relaxation. The dashed line indicates the phase transition from the platic crystalline state to the columnar ordered liquid crystalline phase taken from the analysis of the DC conductivity (see below).

fluctuations within the alkyl side chain, which also involve polar components.

Fig. 18 compares the dielectric spectra for the samples at 90 °C, which is in the temperature range of relaxation process 2. For **c-DOPA(16)·KPF$_6$** a weak peak is observed in the spectra indicating a relaxation process where for **c-THIQ(16)·KPF$_6$** only a shoulder on the low frequency side of the relaxation process 1 is visible. For both materials process 1 and 2 can be separated by analysing the dielectric spectra by fitting the HN-function to the data.[119] This means that for **c-THIQ(16)·KPF$_6$** the intensity of relaxation process 2 is smaller than that of **c-DOPA(16)·KPF$_6$**. The only difference between the samples is that **c-THIQ(16)·KPF$_6$** has no CH_2 bridge in the aromatic core. The CH_2 bridge provides an additional flexibility and mobility to the aromatic

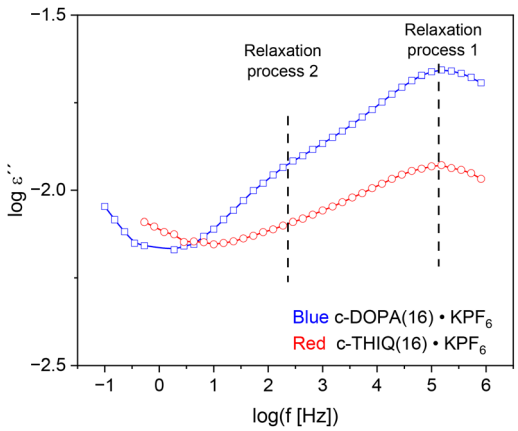

Fig. 18 Dielectric loss *versus* frequency at T = 183.1 K (90 °C): (blue) – **c-DOPA(16)·KPF$_6$**, (red) – **c-THIQ(16)·KPF$_6$**.

core of **c-DOPA(16)·KPF$_6$**. Therefore, the relaxation process 2 is assigned to the small angle rotational or bend fluctuations in the aromatic core. For the sample **c-THIQ(16)·KPF$_6$** the flexibility is restricted leading to a lower intensity. Moreover, relaxation process 2 for **c-THIQ(16)·KPF$_6$** is observed at higher temperatures than that of **c-DOPA(16)·KPF$_6$** (see Fig. 18) supporting the assignment. For the activation energy of relaxation process 2 a value of *ca.* 48 kJ mol^{-1} was estimated for both materials pointing to a localized relaxation process in agreement with the proposed assignment.

The temperature dependence of the relaxation rates of relaxation process 3 also follows the Arrhenius law with estimated apparent activation energies of 70.6 kJ mol^{-1} for **c-DOPA(16)·KPF$_6$** and 59.5 kJ mol^{-1} for **c-THIQ(16)·KPF$_6$**, which are too high for a localized relaxation process. Therefore, it is assumed that relaxation process 3 is due to cooperative processes like glassy dynamics corresponding to a glass transition. As the activation energies of relaxation process 3 for **c-DOPA(16)·KPF$_6$** and **c-THIQ(16)·KPF$_6$** are different it can be further concluded that relaxation process 3 is related to the core and is assigned to the glass transition of the cores. A similar assignment was made also for conventional and ionic liquid crystals.[76,121–123] Due to the CH_2 bridge this process becomes more localized for **c-THIQ(16)·KPF$_6$** in comparison to the **c-DOPA(16)·KPF$_6$** resulting in a lower apparent activation energy.

For **c-DOPA(16)·KPF$_6$** and **c-THIQ(16)·KPF$_6$** a glass transition was detected with conventional DSC as well as with fast scanning calorimetry. As discussed above by a derivative approach it could be proven that a further relaxation (relaxation process 4 or α-relaxation) is hidden under the conductivity contribution for **c-DOPA(16)·KPF$_6$** and **c-THIQ(16)·KPF$_6$**. The analysis of the α-relaxation is given in the SI, Chapter S10 and Fig. S180.

The relaxation rates of relaxation process 4 are included in Fig. 17. The temperature dependence of relaxation process is curved when plotted *versus* invers temperature which can be described by the Vogel/Fulcher/Tammann (VFT-) equation which reads[124–126]

$$\log f_p = \log f_\infty - \frac{A}{T - T_0} \quad (7)$$

The parameter f_∞ represents a pre-exponential factor, A signifies a fitting constant, and the temperature T_0 is the Vogel or ideal glass transition temperature, which is usually found 30–70 K below the glass transition temperature. A VFT temperature dependence of the relaxation rates of a process indicates a glassy dynamics (α-relaxation) taking place here in the hexagonal ordered columnar liquid crystalline phase. The glassy dynamics is connected to a glass transition. It is worth mentioning that the glassy dynamics measured by broadband dielectric spectroscopy is observed in the same temperature range where a glass transition is observed for **c-DOPA(16)·KPF$_6$** and **c-THIQ(16)·KPF$_6$** by fast scanning calorimetry.

The glassy dynamics of **c-DOPA(16)·KPF$_6$** and **c-THIQ(16)·KPF$_6$** is independent of the core. Therefore, it is concluded

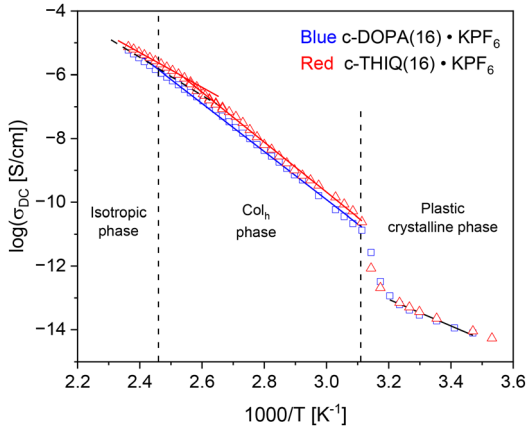

Fig. 19 DC conductivity *versus* invers temperature: (blue squares) – **c-DOPA(16)·KPF$_6$**, (red tringles) – **c-THIQ(16)·KPF$_6$**. The lines are fits of the Arrhenius equation to the corresponding data. Dashed lines indicate the phase transitions temperatures where the phase transition temperatures are taken from DSC.

that the α-relaxation in these compounds is due to the glassy dynamics of alkyl chains in the intercolumnar space.

Due to the salt character of the hybrid materials it is interesting to consider the electrical conductivity. The complex dielectric function is related to the complex conductivity as detailed discussed in the SI, Chapter S10. Examples for the conductivity spectra and the estimation of the electrical DC conductivity σ_{DC} are also given in Fig. S181. As the samples are not oriented between the electrodes the conductivity should be considered as an averaged one.

In Fig. 19 the estimated values for the DC conductivity for **c-DOPA(16)·KPF$_6$** and **c-THIQ(16)·KPF$_6$** are plotted *versus* inverse temperature in Arrhenius coordinates.

In the plastic crystalline phase, the DC conductivity is low, and its temperature dependence is characterized by an Arrhenius law with an activation energy of *ca.* 71 kJ mol^{-1}. In the temperature range of the phase transition from the glass to the hexagonal ordered liquid crystalline phase σ_{DC} changes step-like to higher values. This step-like change in the temperature dependence of σ_{DC} indicates the phase transition. In the temperature range of the hexagonal ordered liquid crystalline phase the DC conductivity increase with increasing temperature also according to the Arrhenius law but with a higher activation energy of *ca.* 154 kJ mol^{-1}. In the temperature range of the Col$_h$ phase to the isotropic phase a decreased activation energy is observed. This change is more pronounced for **c-THIQ(16)·KPF$_6$** in comparison to **c-DOPA(16)·KPF$_6$**.

The DC conductivity values of **c-DOPA(16)·KPF$_6$** and **c-THIQ(16)·KPF$_6$** are similar in the Col$_h$ phase. As the ions in both samples are the same it is concluded that the conductivity in the considered materials is due to drift motions of the mobile anion. Furthermore, the temperature dependence of the DC conductivity follows the Arrhenius law where the temperature dependence of the relaxation rates of the α-relaxation follows the VFT equation. Therefore, the conduction mechanism is not linked to the α-relaxation of the alkyl chains in the intercolumnar space but is due to the drift motion of anions in the channels of the columns formed by the superdiscs.

3. Conclusions

In order to understand the influence of metal salts MX on the liquid crystalline self-assembly as well as molecular mobility, electrical conductivity and long-range orientational order of selected samples within LC cells, two series of amino acid crown ether hybrid materials **c-DOPA(*n*)·MX** (*n* = 12, 14, 16; MX = KSCN, NaI, KI, NaBF$_4$, KBF$_4$, KPF$_6$) and tetrahydroisoquinoline crown ether hybrid materials **c-THIQ(*n*)·KPF$_6$** (*n* = 14, 16) with three linear alkyl side chains were synthesized from L-DOPA. The THIQ series differs from the DOPA series by the presence of a bridging CH$_2$-unit between the aromatic core and the N-terminus resulting in reduced rotational freedom of the amino acid core. Moreover, in the **c-DOPA(*n*)** series hydrogen bonds of the amide unit contribute to the liquid crystalline self-assembly. The investigation of the mesomorphic properties by DSC, POM and XRD revealed that complexation of the crown ether unit with a metal salt is essential for the formation of a mesophase where either SmA$_d$ or Col$_h$ phases were observed. Within the **c-DOPA(*n*)·MX** series (*n* = 12, 14) those complexes with KSCN, NaI, KI, NaBF$_4$ in combination with shorter side chains (*n* = 12, 14) favoured the formation of SmA$_d$ phases, whereas **c-DOPA(*n*)·MX** with long side chains (*n* = 16) favoured the Col$_h$ phase. The results revealed that the combination of chain lengths and anion size is important for the mesophase formation and leads to a "switch" from SmA$_d$ phases for **c-DOPA(14)·KPF$_6$** and **c-THIQ(12)·KPF$_6$** to Col$_h$ states for **c-DOPA(16)·KPF$_6$** and **c-THIQ(14)·KPF$_6$**, respectively.

The choice of the complexation salt also plays a significant role in the stability of the mesophases. All SmA$_d$ phases were monotropic except for the NaI- and KPF$_6$-complexes, which exhibited enantiotropic SmA$_d$ phases. Complexation with NaI in the **c-DOPA(*n*)·MX** series yielded only small mesophase widths of less than 5 K for the hybrid material with short and medium alky chain length (*n* = 12, 14) in the enantiotropic SmA$_d$ phase, while the KPF$_6$ complex significantly stabilized the enantiotropic mesophase, exhibiting the broadest mesophase range with a temperature width of more than 75 K. XRD experiments revealed a bilayer structure of the SmA$_d$ phase with a strong interdigitation of the alkyl chains, deviating from the all-*trans* configuration as well as stacking of the complexed crown ether units in the centre of the bilayer structure. The proposed molecular arrangements within the Col$_h$ phase by superdisc formation of the wedge-shaped mesogens of the **c-DOPA(*n*)·MX** and **c-THIQ(*n*)·MX** series were supported by calculations of electron density maps.

The optical retardation studies show that molecular rigidity plays a decisive role in governing collective alignment in discotic liquid crystals. The non-bridged **c-DOPA(16)·KPF$_6$** displays weak anchoring and multidomain disorder, whereas the bridged **c-THIQ(16)·KPF$_6$** achieves more coherent orientational order and clearer phase transition signatures. The observed

inverse thermal hysteresis further indicates slow relaxation dynamics and interfacial effects influencing phase stability. Overall, covalent rigidification enhances shape persistence and elastic resistance to deformation, providing an effective strategy for improving long-range alignment and optical anisotropy in discotic liquid crystalline materials.

To investigate the conductivity and molecular mobility two selected members **c-DOPA(16)·KPF$_6$** and **c-THIQ(16)·KPF$_6$** of the two series differing only in the presence of the bridging CH_2-unit in their molecular structure were examined by broadband dielectric spectroscopy. These complexes exhibited both a broad enantiotropic Col_h phase in similar temperature ranges. With increasing temperature three low temperature relaxation processes were observed for both complexes, all of which followed the Arrhenius law. The first relaxation process, due to localized fluctuations of the alkyl chains, is independent of the molecular structure of the aromatic core and similar relaxation energies were observed with 35.4 kJ mol^{-1} and 36.6 kJ mol^{-1}, respectively, for both crown ether complexes. The second relaxation process with an estimated activation energy of 48 kJ mol^{-1}, is assigned to a localized relaxation process of the aromatic core. The intensity of process 2 was significantly less for **c-THIQ(16)·KPF$_6$**, due to the constraining effect of the bridging CH_2-unit at the aromatic core. The third relaxation process with activation energies of 70.6 kJ mol^{-1} and 59.5 kJ mol^{-1}, respectively, is related to a glass transition of the aromatic cores, which due to the bridging CH_2-unit is more localized for **c-THIQ(16)·KPF$_6$**, resulting in a lower activation energy. Finally, in the temperature region of the glass transition a fourth relaxation process was observed for both complexes, which was independent of the aromatic core and followed the VFT-temperature dependence. The process was assigned to glassy dynamics (α-relaxation) of the alkyl chains in the intercolumnar space.

For both complexes electrical conductivity was observed in the dielectric loss spectra. The temperature dependence estimated DC followed the Arrhenius law upon heating from the plastic crystalline phase a step wise increase of conductivity was observed. In the mesophases an activation energy of approximately 154 kJ mol^{-1} was estimated for both complexes. Further heating into the isotropic state resulted in a slight decrease of the activation energy, which was slightly more pronounced for **c-THIQ(16)·KPF$_6$**. The conductivity was attributed to the drift motion of the PF_6^- anions within the channels formed by columnar structures of the mesophase, as for both complexes the activation energy was independent of the presence of the CH_2-bridging unit.

Our results have shown that salt complexation controls both self-assembly and induces ion transport in amino acid crown ether hybrids, paving the way towards ion-conducting applications.

Author contributions

A. R. R. conceived the project and did a part of the synthesis, most of the characterization, analysis and data curation and wrote the first draft of the manuscript. T. R. G. did a part of the synthesis and characterization. P. S. and A. S. supervised the dielectric measurement. D. R. performed a part of the dielectric measurements and the fast-scanning calorimetry experiments and reviewed the manuscript. P. S. and A. S. contributed their expertise regarding analysis of the dielectric measurement. A. S. helped with the manuscript preparation and checked the data. Z. L. performed the optical retardation studies and helped with the manuscript preparation. A. Z. checked the data and helped with the manuscript preparation. P. H. contributed his expertise regarding XRD analysis. J. R. B. assisted with conceiving the packing models and calculating electron densities. S. L supervised the project and wrote the manuscript. All co-authors checked and proofread the final version of the manuscript.

Conflicts of interest

There are no conflicts to declare.

Data availability

All data supporting the findings of this publication are included in the supplementary information (SI) file accompanying this article. Supplementary information: ^{1}H NMR and ^{13}C NMR and ^{19}F NMR spectra; details of X-Ray diffraction, DSC, FSC, POM, retardation and dielectric measurements. See DOI: https://doi.org/10.1039/d5tc04129e.

Acknowledgements

Marcel Freund assisted in conceiving the synthesis. Soeren M. Bauch and Sebastian B. Wachsmann conceived a plug-in utilized in the software for the analysis. Generous financial support by the Deutsche Forschungsgemeinschaft (DFG grant # LA 907/21-1; HU 850/13-1; SCHO 470/26-1, INST 41/897-1 FUGG for 700 MHz NMR, INST 41/1136-1 FUGG for Orbitrap LC-MS), the Carl-Schneider Stiftung Aalen (shared instrumentation grant) and the Ministerium für Wissenschaft, Forschung und Kunst des Landes Baden-Württemberg are gratefully acknowledged.

Notes and references

1 T. Öztepe, N. B. Kale, T. Reçber, İ. Baysal, S. Yabanoğlu-Çiftçi, M. Gumustas, S. Kır, B. Chankvetadze and E. Nemutlu, *J. Chromatogr. A*, 2022, **1683**, 463529.
2 T. Németh, G. Dargó, J. L. Petró, Z. Petrik, S. Lévai, B. Krámos, Z. Béni, J. Nagy, G. T. Balogh, P. Huszthy and T. Tóth, *Chirality*, 2017, **29**, 522–535.
3 E. S. Cho, J. Y. Sung, J. S. Jin and M. H. Hyun, *J. Sep. Sci.*, 2018, **41**, 1192–1198.
4 T. Upmanis and H. Kažoka, *J. Chromatogr. A*, 2022, **1673**, 463059.
5 R. Berkecz, G. Németi, A. Péter and I. Ilisz, *Molecules*, 2021, **26**, 4648.

6 I. Kawamura, B. Mijiddorj, Y. Kayano, Y. Matsuo, Y. Ozawa, K. Ueda and H. Sato, *Biochim. Biophys. Acta, Proteins Proteomics*, 2020, **1868**, 140429.
7 G. Carenzi, S. Sacchi, M. Abbondi and L. Pollegioni, *Amino Acids*, 2020, **52**, 849–862.
8 K. Hirose, J. Yongzhu, T. Nakamura, R. Nishioka, T. Ueshige and Y. Tobe, *J. Chromatogr. A*, 2005, **1078**, 35–41.
9 P. Gerbaux, J. De Winter, D. Cornil, K. Ravicini, G. Pesesse, J. Cornil and R. Flammang, *Chem. – Eur. J.*, 2008, **14**, 11039–11049.
10 Y. Konya, M. Taniguchi, M. Furuno, Y. Nakano, N. Tanaka and E. Fukusaki, *J. Chromatogr. A*, 2018, **1578**, 35–44.
11 K. Yoshikawa, M. Furuno, N. Tanaka and E. Fukusaki, *J. Biosci. Bioeng.*, 2020, **130**, 437–442.
12 C. Yuan, W. Jia, Z. Yu, Y. Li, M. Zi, L. M. Yuan and Y. Cui, *J. Am. Chem. Soc.*, 2022, **144**, 891–900.
13 J. Y. Sung, S. M. Jin, S. Lee, S. Y. An and J. S. Jin, *Talanta*, 2021, **235**, 122739.
14 Y. Nakano, M. Taniguchi and E. Fukusaki, *J. Biosci. Bioeng.*, 2019, **127**, 520–527.
15 L. Miller and L. Yue, *Chirality*, 2020, **32**, 981–989.
16 Y. Konya, Y. Izumi, K. Hamase and T. Bamba, *J. Chromatogr. A*, 2022, **1677**, 463305.
17 S. Lee, S. J. Kim, E. Bang and Y. C. Na, *J. Chromatogr. A*, 2019, **1586**, 128–138.
18 F. E. O. Suliman, S. K. Al Burtomani, A. A. Elbashir and O. J. Schmitz, *Electrophoresis*, 2021, **42**, 1800–1809.
19 K. Tsubaki, D. Tanima, M. Nuruzzaman, T. Kusumoto, K. Fuji and T. Kawabata, *J. Org. Chem.*, 2005, **70**, 4609–4616.
20 Y. Chen and M. T. Rodgers, *J. Am. Chem. Soc.*, 2012, **134**, 5863–5875.
21 Y. Chen and M. T. Rodgers, *J. Am. Chem. Soc.*, 2012, **134**, 2313–2324.
22 M. Kruppa, C. Mandl, S. Miltschitzky and B. König, *J. Am. Chem. Soc.*, 2005, **127**, 3362–3365.
23 Á. Golcs, B. Á. Ádám, V. Horváth, T. Tóth and P. Huszthy, *Molecules*, 2020, **25**, 2571.
24 O. H. Rubio, R. Taouil, F. M. Muñiz, L. M. Monleón, L. Simón, F. Sanz and J. R. Morán, *Org. Biomol. Chem.*, 2017, **15**, 477–485.
25 H. Ma, D. Luo, Q. Zhao, R. Liu, Z. Zhang, X. Hou, X. Sun and Y. Wang, *J. Mol. Liq.*, 2022, **345**, 117884.
26 Q. Y. Feng, S. Tong, S. Z. Vatsadze and M. X. Wang, *Tetrahedron*, 2023, **131**, 133207.
27 Y. C. Rodriguez, T. M. Duarte, Z. Szakonyi, E. Forrõ, F. Fülöp and T. J. Wenzel, *Chirality*, 2015, **27**, 708–715.
28 J. R. Avilés-Moreno, G. Berden, J. Oomens and B. Martínez-Haya, *Phys. Chem. Chem. Phys.*, 2018, **20**, 4067–4073.
29 J. R. Avilés-Moreno, G. Berden, J. Oomens and B. Martínez-Haya, *Phys. Chem. Chem. Phys.*, 2017, **19**, 31345–31351.
30 C. P. McNary, Y. W. Nei, P. Maitre, M. T. Rodgers and P. B. Armentrout, *Phys. Chem. Chem. Phys.*, 2019, **21**, 12625–12639.
31 D. Jagleniec, N. Walczak, Ł. Dobrzycki and J. Romański, *Int. J. Mol. Sci.*, 2021, **22**, 10754.
32 P. Dominique, M. Schnurr and B. Lewandowski, *Chem. Commun.*, 2021, **57**, 3476–3479.
33 A. Weißenstein, C. R. Saha-Möller and F. Würthner, *Chem. – Eur. J.*, 2018, **24**, 8009–8016.
34 F. Oukhatar, S. Même, W. Même, F. Szeremeta, N. K. Logothetis, G. Angelovski and É. Tóth, *ACS Chem. Neurosci.*, 2015, **6**, 219–225.
35 F. Oukhatar, H. Meudal, C. Landon, N. K. Logothetis, C. Platas-Iglesias, G. Angelovski and É. Tóth, *Chem. – Eur. J.*, 2015, **21**, 11226–11237.
36 N. F. Atta, A. Galal and Y. M. Ahmed, *J. Electrochem. Soc.*, 2019, **166**, B623–B630.
37 N. F. Atta, Y. M. Ahmed and A. Galal, *Electroanalysis*, 2019, **31**, 1204–1214.
38 Y. Luo, N. Marets and T. Kato, *Chem. Sci.*, 2018, **9**, 608–616.
39 F. Otis, M. Auger and N. Voyer, *Acc. Chem. Res.*, 2013, **46**, 2934–2943.
40 J. Shen, R. Ye and H. Zeng, *Angew. Chem., Int. Ed.*, 2021, **60**, 12924–12930.
41 Y. Li, J. Dong, W. Gong, X. Tang, Y. Liu, Y. Cui and Y. Liu, *J. Am. Chem. Soc.*, 2021, **143**, 20939–20951.
42 P. A. Paquet-Côté, J. P. Paradis, M. Auger and N. Voyer, *Biochim. Biophys. Acta, Biomembr.*, 2020, **1862**, 183261.
43 M. Lehmann, P. Weinberger, M. Finze, G. A. Giffin, M. Weller, S. Bachmann and A. C. Pöppler, *J. Mater. Chem. C*, 2024, **12**, 7233–7239.
44 V. Conejo-Rodríguez, C. Cuerva, R. Schmidt, M. Bardají and P. Espinet, *J. Mater. Chem. C*, 2019, **7**, 663–672.
45 T. Wöhrle, I. Wurzbach, J. Kirres, A. Kostidou, N. Kapernaum, J. Litterscheidt, J. C. Haenle, P. Staffeld, A. Baro, F. Giesselmann and S. Laschat, *Chem. Rev.*, 2016, **116**, 1139–1241.
46 I. Carrasco, P. Ehni, M. Ebert, N. Dumait, G. Taupier, M. Amela-Cortes, C. Roiland, S. Cordier, J. A. Knöller, E. Jacques, S. Laschat and Y. Molard, *ACS Appl. Mater. Interfaces*, 2023, **15**, 39752–39764.
47 P. Staffeld, M. Kaller, P. Ehni, M. Ebert, S. Laschat and F. Giesselmann, *Crystals*, 2019, **9**, 74.
48 K. Guy, P. Ehni, S. Paofai, R. Forschner, C. Roiland, M. Amela-Cortes, S. Cordier, S. Laschat and Y. Molard, *Angew. Chem., Int. Ed.*, 2018, **57**, 11692–11696.
49 J. Kirres, K. Schmitt, I. Wurzbach, F. Giesselmann, S. Ludwigs, M. Ringenberg, A. Ruff, A. Baro and S. Laschat, *Org. Chem. Front.*, 2017, **4**, 790–803.
50 P. Ehni, K. Guy, M. Ebert, S. Beardsworth, K. Bader, R. Forschner, A. Bühlmeyer, N. Dumait, C. Roiland, Y. Molard and S. Laschat, *Dalton Trans.*, 2018, **47**, 14340–14351.
51 J. Li, Z. He, H. Gopee and A. N. Cammidge, *Org. Lett.*, 2010, **12**, 472–475.
52 U. Beginn, G. Zipp and M. Möller, *Adv. Mater.*, 2000, **12**, 510–513.
53 U. Beginn, G. Zipp and M. Möller, *Chem. – Eur. J.*, 2000, **6**, 2016–2023.
54 U. Beginn, G. Zipp, A. Mourran, P. Walther and M. Möller, *Adv. Mater.*, 2000, **12**, 513–516.

55 G. Johansson, V. Percec, G. Ungar and D. Abramic, *J. Chem. Soc., Perkin Trans. 1*, 1994, 447.
56 G. Ungar, S. V. Batty, V. Percec, J. Heck and G. Johansson, *Adv. Mater. Opt. Electron.*, 1994, **4**, 303–313.
57 V. Percec, G. Johansson, J. Heck, G. Ungarb and S. V. Battyb, *J. Chem. Soc., Perkin Trans. 1*, 1993, 1411.
58 T. Basova, F. Latteyer, D. Atilla, A. G. Gürek, A. Hassan, V. Ahsen, H. Peisert and T. Chassè, *Thin Solid Films*, 2010, **518**, 5745–5752.
59 C. W. Ong, C. Q. Yan, M.-C. Yeh and M.-C. Tzeng, *Mol. Cryst. Liq. Cryst.*, 2015, **610**, 249–254.
60 B. Zhang, J. Wang, Z.-Q. Yu, S. Yang, A.-C. Shi and E.-Q. Chen, *J. Mater. Chem. C*, 2014, **2**, 5168.
61 V. Percec, G. Zipp, G. Johansson, U. Beginn and M. Möller, *Macromol. Chem. Phys.*, 1997, **198**, 265–277.
62 U. Beginn, G. Zipp, M. Möller, G. Johansson and V. Percec, *Macromol. Chem. Phys.*, 1997, **198**, 2839–2852.
63 M. M. Neidhardt, M. Wolfrum, S. Beardsworth, T. Wöhrle, W. Frey, A. Baro, C. Stubenrauch, F. Giesselmann and S. Laschat, *Chem. – Eur. J.*, 2016, **22**, 16494–16504.
64 K. Bader, M. M. Neidhardt, T. Wöhrle, R. Forschner, A. Baro, F. Giesselmann and S. Laschat, *Soft Matter*, 2017, **13**, 8379–8391.
65 M. M. Neidhardt, K. Schmitt, A. Baro, C. Schneider, U. Bilitewski and S. Laschat, *Phys. Chem. Chem. Phys.*, 2018, **20**, 20371–20381.
66 M. A. Grunwald, S. E. Hagenlocher, L. Turkanovic, S. M. Bauch, S. B. Wachsmann, L. A. Altevogt, M. Ebert, J. A. Knöller, A. R. Raab, F. Schulz, M. A. Kolmangadi, A. Zens, P. Huber, A. Schönhals, U. Bilitiewski and S. Laschat, *Phys. Chem. Chem. Phys.*, 2023, **25**, 17639–17656.
67 Z. Li, A. Raab, M. A. Kolmangadi, M. Busch, M. Grunwald, F. Demel, F. Bertram, A. V. Kityk, A. Schönhals, S. Laschat and P. Huber, *ACS Nano*, 2024, **18**, 14414–14426.
68 Z. Huang, J. Zhang, Y. Liu, A. Song and J. Hao, *J. Mol. Liq.*, 2020, **301**, 112399.
69 S. Fujiwara, H. Ohno, M. Yoshio, T. Kato and T. Ichikawa, *Bull. Chem. Soc. Jpn.*, 2018, **91**, 1–5.
70 S. Fujiwara, H. Ohno and T. Ichikawa, *Mol. Syst. Des. Eng.*, 2018, **3**, 668–676.
71 K. Fujimura, T. Ichikawa, M. Yoshio, T. Kato and H. Ohno, *Chem. – Asian J.*, 2016, **11**, 520–526.
72 T. Ichikawa, K. Fujimura, M. Yoshio, T. Kato and H. Ohno, *Chem. Commun.*, 2013, **49**, 11746.
73 S. Z. Mohammady, M. Pouzot and R. Mezzenga, *Biophys. J.*, 2009, **96**, 1537–1546.
74 R. Mezzenga, J. M. Seddon, C. J. Drummond, B. J. Boyd, G. E. Schröder-Turk and L. Sagalowicz, *Adv. Mater.*, 2019, **31**, 1900818.
75 M. A. Kolmangadi, A. R. Raab, P. Szymoniak, Z. Li, P. Huber, S. Laschat and A. Schönhals, *Phys. Chem. Chem. Phys.*, 2025, **27**, 18162–18178.
76 M. A. Kolmangadi, A. Yildirim, K. Sentker, M. Butschies, A. Bühlmeyer, P. Huber, S. Laschat and A. Schönhals, *J. Mol. Liq.*, 2021, **330**, 115666.
77 C. J. Pedersen, *Angew. Chem.*, 1988, **100**, 1053–1059.
78 L. X. Dang, *J. Am. Chem. Soc.*, 1995, **117**, 6954–6960.
79 G. J. Yuan, Y. T. Luan, J. Bin Miao, C. F. Wang, L. Chen, C. Chen, H. Chen, L. Li and X. M. Ren, *Eur. J. Inorg. Chem.*, 2023, e202300523.
80 J. W. Steed, *Coord. Chem. Rev.*, 2001, **215**, 171–221.
81 R. G. Pearson, *Inorg. Chim. Acta*, 1995, **240**, 93–98.
82 P. W. Ayers, M. Mohamed and F. Heidar-Zadeh, *Conceptual Density Functional Theory: Towards a New Chemical Reactivity Theory*, Wiley-VCH, Weinheim, 2022, vol. 2.
83 C. Haege, S. Jagiella and F. Giesselmann, *Chem. Phys. Chem.*, 2019, **20**, 2466–2472.
84 G. W. Stewart, *Phys. Rev.*, 1928, **32**, 558–563.
85 M. D. Hanwell, D. E. Curtis, D. C. Lonie, T. Vandermeersch, E. Zurek and G. R. Hutchison, *J. Cheminform.*, 2012, **4**, 17.
86 N. Kapernaum, C. Müller, S. Moors, M. C. Schlick, E. Wuckert, S. Laschat and F. Giesselmann, *Chem. Phys. Chem.*, 2016, **17**, 4116–4123.
87 A. De Vries, *Mol. Cryst. Liq. Cryst.*, 1970, **11**, 361–383.
88 A. De Vries, *Mol. Cryst. Liq. Cryst.*, 1977, **41**, 27–31.
89 K. Bader, C. Müller, Y. Molard, A. Baro, P. Ehni, J. Knelles and S. Laschat, *RSC Adv.*, 2020, **10**, 23999–24016.
90 F. Schulz, B. Wank, P. Nacke, W. Frey and S. Laschat, *Mater. Adv.*, 2023, **4**, 1306–1313.
91 F. Schulz, B. Lutz, D. Rück, D. Batman, W. Frey and S. Laschat, *Soft Matter*, 2023, **19**, 2397–2406.
92 D. R. Rueda, A. Nogales, J. J. Hernández, M. C. García-Gutiérrez, T. A. Ezquerra, S. V. Roth, M. G. Zolotukhin and R. Serna, *Langmuir*, 2007, **23**, 12677–12681.
93 L. Yuan, J. Zhu, S. Wu and C. Chi, *Chem. Commun.*, 2022, **58**, 1302–1305.
94 P. Davidson and L. Strzelecki, *Liq. Cryst.*, 1988, **3**, 1583–1595.
95 D. M. Smilgies, *Rev. Sci. Instrum.*, 2002, **73**, 1706–1710.
96 S. Aeffner, T. Reusch, B. Weinhausen and T. Salditt, *Eur. Phys. J. E.*, 2009, **30**, 205–214.
97 S. Laschat, A. Baro, N. Steinke, F. Giesselmann, C. Hägele, G. Scalia, R. Judele, E. Kapatsina, S. Sauer, A. Schreivogel and M. Tosoni, *Angew. Chem., Int. Ed.*, 2007, **46**, 4832–4887.
98 E. Grelet, S. Dardel, H. Bock, M. Goldmann, E. Lacaze and F. Nallet, *Eur. Phys. J. E.*, 2010, **31**, 343–349.
99 V. Percec, C. M. Mitchell, W. D. Cho, S. Uchida, M. Glodde, G. Ungar, X. Zeng, Y. Liu, V. S. K. Balagurusamy and P. A. Heiney, *J. Am. Chem. Soc.*, 2004, **126**, 6078–6094.
100 J. Xu, *ACS Mater. Au*, 2023, **3**, 450–455.
101 K. V. Axenov and S. Laschat, *Materials*, 2010, **4**, 206–259.
102 L. Douce, J. M. Suisse, D. Guillon and A. Taubert, *Liq. Cryst.*, 2011, **38**, 1653–1661.
103 T. Kato and M. Yoshio, Liquid Crystalline Ionic Liquids, in *Electrochemical Aspects of Ionic Liquids*, ed. H. Ohno, John Wiley & Sons, Hoboken, 2011, pp. 307–320.
104 S. Chen and S. H. Eichhorn, *Isr. J. Chem.*, 2012, **52**, 830–843.
105 V. Causin and G. Saielli, Ionic Liquid Crystals, in *Green Solvents II: Properties and Applications of Ionic Liquids*, ed. A. Mohammad and D. Inamuddin, Springer, Dordrecht, 2012, pp. 79–118.

106 M. Mansueto and S. Laschat, Ionic Liquid Crystals, in *Handbook of Liquid Crystals*, ed. J. W. Goodby, C. Tschierske, P. Raynes, H. Gleeson, T. Kato and P. J. Collings, Wiley-VCH, Weinheim, 2014, vol. 6.
107 K. Goossens, K. Lava, C. W. Bielawski and K. Binnemans, *Chem. Rev.*, 2016, **116**, 4643–4807.
108 S. J. Devaki and R. Sasi, Ionic Liquids/Ionic Liquid Crystals for Safe and Sustainable Energy Storage Systems, in *Progress and Developments in Ionic Liquids*, ed. S. Handy, Intech, 2017.
109 V. Cîrcu, Ionic Liquid Crystals Based on Pyridinium Salts, in *Progress and Developments in Ionic Liquids*, ed. S. Handy, Intech, 2017.
110 T. Ichikawa, T. Kato and H. Ohno, *Chem. Commun.*, 2019, **55**, 8205–8214.
111 K. Salikolimi, A. A. Sudhakar and Y. Ishida, *Langmuir*, 2020, **36**, 11702–11731.
112 K. Sentker, A. Yildirim, M. Lippmann, A. W. Zantop, F. Bertram, T. Hofmann, O. H. Seeck, A. V. Kityk, M. G. Mazza, A. Schönhals and P. Huber, *Nanoscale*, 2019, **11**, 23304–23317.
113 A. V. Kityk, M. Wolff, K. Knorr, D. Morineau, R. Lefort and P. Huber, *Phys. Rev. Lett.*, 2008, **101**, 187801.
114 C. Tschierske, *Angew. Chem., Int. Ed.*, 2013, **52**, 8828–8878.
115 P. G. de Gennes and J. Prost, *The physics of liquid crystals*, Clarendon Press, 2001.
116 S. Das, A. Mondal and C. M. Reddy, *Chem. Soc. Rev.*, 2020, **49**, 8878–8896.
117 S. Havriliak and S. Negami, *J. Polym. Sci. C, Polym. Symp.*, 1966, **14**, 99–117.
118 M. Wübbenhorst and J. van Turnhout, *J. Non-Cryst. Solids*, 2002, **305**, 40–49.
119 A. Schönhals and F. Kremer, Analysis of Dielectric Spectra, in *Broadband Dielectric Spectroscopy*, ed. F. Kremer and A. Schönhals, Springer, Berlin, Heidelberg, 2003, pp. 59–98.
120 O. Van Den Berg, W. G. F. Sengers, W. F. Jager, S. J. Picken and M. Wübbenhorst, *Macromolecules*, 2004, **37**, 2460–2470.
121 A. Yildirim, C. Krause, P. Huber and A. Schönhals, *J. Mol. Liq.*, 2022, **358**, 119212.
122 A. Yildirim, M. A. Kolmangadi, A. Buhlmeyer, P. Huber, S. Laschat and A. Schönhals, *J. Phys. Chem. B*, 2020, **124**, 8728–8739.
123 M. A. Kolmangadi, G. J. Smales, L. Zhuoqing, A. Yildirim, E. Wuckert, S. Eutionnat, F. Demel, P. Huber, S. Laschat and A. Schönhals, *J. Phys. Chem. C*, 2022, **126**, 10995–11006.
124 H. Vogel, *Phys. Z.*, 1921, **22**, 645–646.
125 G. S. Fulcher, *J. Am. Ceram. Soc.*, 1925, **8**, 339–355.
126 G. Tammann and W. Hesse, *Z. Anorg. Allg. Chem.*, 1926, **156**, 245–257.